

## TOPICAL REVIEW

# Antenna–load interactions at optical frequencies: impedance matching to quantum systems

R L Olmon and M B Raschke

Department of Physics, Department of Chemistry, and JILA, University of Colorado, Boulder, CO 80309, USA

E-mail: [markus.raschke@colorado.edu](mailto:markus.raschke@colorado.edu)

Received 16 April 2012, in final form 2 July 2012

Published 18 October 2012

Online at [stacks.iop.org/Nano/23/444001](http://stacks.iop.org/Nano/23/444001)

## Abstract

The goal of antenna design at optical frequencies is to deliver optical electromagnetic energy to loads in the form of, e.g., atoms, molecules or nanostructures, or to enhance the radiative emission from such structures, or both. A true optical antenna would, on a qualitatively new level, control the light–matter interaction on the nanoscale for controlled optical signal transduction, radiative decay engineering, quantum coherent control, and super-resolution microscopy, and provide unprecedented sensitivity in spectroscopy. Resonant metallic structures have successfully been designed to approach these goals. They are called optical antennas in analogy to radiofrequency (RF) antennas due to their capability to collect and control electromagnetic fields at optical frequencies. However, in contrast to the RF, where exact design rules for antennas, waveguides, and antenna–load matching in terms of their impedances are well established, substantial physical differences limit the simple extension of the RF concepts into the optical regime. Key distinctions include, for one, intrinsic material resonances including quantum state excitations (metals, metal oxides, semiconductor homo- and heterostructures) and extrinsic resonances (surface plasmon/phonon polaritons) at optical frequencies. Second, in the absence of discrete inductors, capacitors, and resistors, new design strategies must be developed to impedance match the antenna to the load, ultimately in the form of a vibrational, electronic, or spin excitation on the quantum level. Third, there is as yet a lack of standard performance metrics for characterizing, comparing and quantifying optical antenna performance. Therefore, optical antenna development is currently challenged at all the levels of design, fabrication, and characterization.

Here we generalize the ideal antenna–load interaction at optical frequencies, characterized by three main steps: (i) far-field reception of a propagating mode exciting an antenna resonance, (ii) subsequent transformation of that mode into a nanoscale spatial localization, and (iii) near-field coupling via an enhanced local density of states to a quantum load. These three steps define the goal of efficient transformation of incident radiation into a quantum excitation in an impedance-matched fashion. We review the physical basis of the light–matter interaction at the transition from the RF to optical regime, discuss the extension of antenna theory as needed for the design of impedance-matched optical antenna–load coupled systems, and provide several examples of the state of the art in design strategies and suggest future extensions. We furthermore suggest new performance metrics based on the combination of electric vector field, field enhancement and capture cross section measurement to aid in comparison between different antenna designs and optimization of optical antenna performance within the physical parameter space.

(Some figures may appear in colour only in the online journal)

## 1. Introduction

Electromagnetic (EM) waves from low radiofrequencies (RF) to high optical frequencies pervade our environment. They interact with matter by coupling directly to the motion of charge carriers. This carrier motion can be associated with characteristic spectral resonances resulting from absorption and emission of EM energy. These resonances can be broken into two types. Intrinsic resonances reflect underlying material parameters related to the electronic and lattice structure of the constituent matter, its chemical bonds, and crystallographic and symmetry properties [1, 2]. Extrinsic resonances, on the other hand, are dependent on the size, geometry, and material composition of an object. Devices can be engineered with extrinsic resonances defined with respect to oscillator strength, bandwidth, and resonant frequency [3–5].

A common implementation of resonance engineering is the RF antenna operating in the  $10^3$ – $10^{11}$  Hz range [6–10]. According to the *IEEE Standard Definitions of Terms for Antennas*, an antenna is defined as the ‘part of a transmitting or receiving system that is designed to radiate or to receive electromagnetic waves’ [11]. Depending on the resonance properties, environment, and use, an antenna can be designed in all sizes and shapes including linear dipoles, horns, dishes, apertures, and patches. Despite the different form factors, all antennas operate under the same principle. They mediate the transformation between propagating EM energy and localized or confined energy delivered to a load or emitted from a source via coupling of the EM energy to electron motion.

Although originally conceived for radio waves, the antenna definition above notably does not constrain the frequency range of operation. The same transformation principle could conceptually be expanded to optical frequencies. As has been observed in the field of silicon electronics, device size can be scaled down by orders of magnitude provided the physical mechanisms underlying the device operation remain the same. However, despite great interest and several attempts to scale the rich tool set developed for RF antenna design to optical frequencies, there is a qualitative change in interaction and physical principles below the millimetre range. RF antennas operate in the Hagen–Rubens frequency regime where the frequency of operation is much less than the Drude–Sommerfeld electron relaxation rate and optical properties are largely defined by the dc conductivity. However, for metals at optical frequencies the imaginary part of the conductivity exceeds the real part, and the magnitude of the real part of the dielectric function decreases significantly with frequency [1]. Consequently, as shown in figure 1, extrinsic resonances become the result of, e.g., surface-bound localized plasmon polaritons rather than loosely bound antenna current resonances. Moreover, with device size defined by the wavelength of operation  $\lambda$ , the feature sizes of plasmonic antennas are on the order of 10–100 nm, comparable to the length scales of the elementary intrinsic excitations. The Drude–Sommerfeld mean free path, or distance between scattering events of free electrons in gold, for example, is about 30 nm [2], which can give rise to finite-size effects and deviations from bulk-like material

response. Scaling antenna technology to the optical regime is thus associated with the emergence of frequency-dependent material parameters, increased Ohmic loss, different length scales and proximity ranges of interest, and the resulting inapplicability of many assumptions and approximations often used in RF antenna design and analysis. Many years of antenna design extrapolating RF concepts have shown that the different physical mechanisms at work including the four orders of magnitude conductivity difference in metals between RF and optical frequencies calls for a qualitatively different approach.

Despite the different physical mechanisms at optical frequencies, or indeed, in part because of them, nanometre and micrometre sized metallic structures have demonstrated some capability to collect, control, and confine optical EM fields. Thus they have been called ‘optical antennas’ in analogy to their RF counterparts [14–21]. Many proposed optical antennas take advantage of the high local charge densities associated with, e.g., plasmonic lenses [22–24], plasmonic waveguides [25–30], or resonant metallic particles to create local (near-field) electromagnetic fields enhanced in intensity with respect to an incident excitation field. These resonant metallic structures have found some applications in the IR and visible regimes in the fields of optical sensing [13, 31–35], biosensing [36–38], plasmonics [39–44], optical microscopy and nanoscopy [45–51], microspectroscopy [30, 52, 53], and radiative decay engineering [54–65], among others.

Nevertheless, there seem to be several misconceptions regarding the applicability and limitations of the different analyses drawn between optical and RF antennas. RF antenna design benefits from standard materials, methods, and tools such as discrete resistive, capacitive, and inductive elements and conventional feed mechanisms that do not exist for optical antennas, necessitating different design strategies which have yet to be developed. Nor does optical antenna design have a standard metric by which the performance of different antennas may be compared. Optical antennas can be characterized by field enhancement, but this fails to account for capture efficiency, footprint, Ohmic losses, etc.

The ultimate goal in the development of optical antennas is to facilitate the delivery of light to nanoscale receivers (or reciprocally the emission from sources). This delivery should be efficient in terms of total captured power and minimal transmission or transformation loss. A high performance optical antenna would allow for a qualitatively new level of control of e.g. the light–matter interaction. The application of such optical antennas would enhance or enable nanoscale signal transduction, radiative decay engineering, quantum coherent control, super-resolution microscopy, and unprecedented sensitivity in a broad range of spectroscopies.

An antenna must capture light and prepare it for delivery to a load. The generalized ideal system would perform the following functions (given here for a system in receiving mode): (i) reception of far-field propagating light exciting an extrinsic antenna resonance and (ii) subsequent transformation of that mode into a confined spatial localization. These two functions closely resemble the RF analogue. Interconnecting electronic circuitry used to

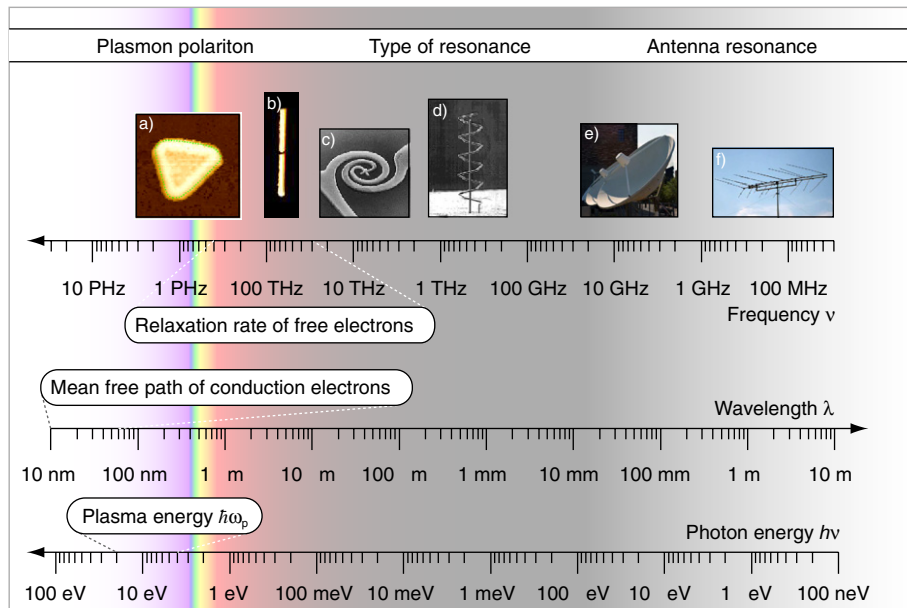


**Figure 1.** Scaling of antennas from radio to optical frequencies. Optical antennas inhabit the infrared and visible frequency regimes, from around 10 THz to 1 PHz. Antennas in this range have dimensions and structural features that are on the size scale of the mean free path of electrons, and resonance frequencies approximately equal to the electron relaxation rate. Consequently, new effects not seen for RF antennas associated with the lower real conductivity of the metal arise at high frequencies, including greater absorptive losses, modified effective wavelength scaling, and changes in the radiative emission rate. (a) Silver nanoprism optical antenna adapted from [12]. Copyright 2008 American Chemical Society. (b) Linear coupled dimer optical antenna. (c) IR spiral antenna reprinted from [13] with permission from Elsevier, copyright 1998. (d) 3D Helical THz antenna reprinted from [175] with permission from John Wiley and Sons, copyright 2000. (e) Television uplink dish antenna. (f) Radio wire antenna.

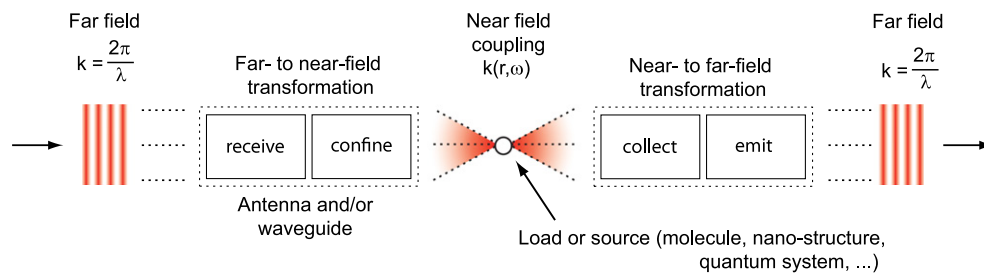


**Figure 2.** The receive–transform–couple (RTC) scheme for energy delivery to a nanoload, and the complementary scheme for extraction of energy from a source. A far- to near-field transformation device optimizes the interaction between the propagating light and the nano-optical element. Similarly, light emission by a nano-optical device can be enhanced in terms of the radiative rate by using a near- to far-field transformer to mediate energy transfer into propagating modes.

connect RF components is not available for optical antennas, however. Instead, optical electromagnetic interactions have to be controlled via the local density of states (LDOS) [61, 66]. Energy delivery to a load may occur through an electromagnetic near-field interaction. Thus we add a third function to the general model, namely near-field coupling via an enhanced local density of states to a quantum load.

Some of these concepts have been discussed previously in specific contexts. Figure 2 shows our generalization of these concepts which may help bring optical antenna design onto a common footing, serving as a reference and benchmark by which different light transformation strategies may be compared. Far-field propagating EM energy is received and concentrated by a transforming device for coupling to a load. This constitutes a receive–transform–couple (RTC) delivery scheme which will be a major theme of this work. The

transforming device may consist of a single element or two coupled elements (for example a coupler and a waveguide). In the optical frequency regime, the load may also be a molecule, atom, quantum dot, or metallic particle, for example, instead of an electronic circuit as in the RF case. A similar transformation can assist the reverse process, namely collecting energy from a source and emitting it radiatively.

Many excellent reviews have discussed the state of the art in optical antennas [14–20]. Here we attempt to provide a more generalized perspective addressing several fundamental aspects. We consider optical nanofocusing devices in the context of the ultimate goal of providing a highly efficient method for delivering light to the nanoscale. We give a critical account of the state of the art of the design of impedance-matched optical antenna-coupled systems. This includes a discussion of different ways to describe impedance

and impedance matching, including more conventional input impedance descriptions as well as interaction through the local density of states where antenna–load coupling occurs through the near-field. We note general limitations, special requirements, and areas where more investigation is merited in order to develop more efficient optoelectronic devices. We compare and contrast antennas with excitation and radiative emission of quantum systems. We extend the discussion to the ability of antennas to control optical excitations in the temporal domain down to the femtosecond timescale.

The paper is organized as follows: first we discuss linear antenna resonances and impedance in order to provide a basis for the discussion of the extension of RF designs to optical frequencies. Next we highlight the different physical mechanisms at work between RF and optical antennas through a discussion of the properties of metals at optical frequencies where conductivity is characterized by a decreasing real part and substantial imaginary part. The implications of the geometric and material differences between RF and optical frequency antennas are then examined in the context of reception of incident light via extrinsic optical antenna resonances governed by surface plasmon/phonon polaritons. Next, we examine energy transformation and coupling to a load, in terms of suggested methods for dealing with impedance of optical antennas using input impedance at an antenna gap. Then we consider light–matter interactions at the nanoscale through a quantum level description and discuss the competition between radiative and nonradiative excitation decay channels in antennas and quantum emitters. Using the example of a new type of antenna in the form of a metal cone, we demonstrate how standardized optical antenna parameter characterization can aid comparisons between different architectures in the RTC paradigm. The final section reports on our measurement techniques of near-field mapping and characterization of field enhancement of optical antennas to assign performance metrics that can evaluate the performance of each stage of the RTC process. In particular, we focus on the nano-optical vector network analyser for full EM characterization.

## 2. Radiofrequency antennas

The electromagnetic properties, geometry, material parameters, and resonance characteristics of an antenna are intrinsically linked. This section discusses how resonance is related to antenna impedance. We examine antennas as they are analysed in the RF for two reasons. First, this provides a basis for nomenclature and expectations that we shall apply to optical antennas. Second, the maturity of understanding of RF antennas and the cohesiveness of analytical and measurement techniques set standards that shall be adopted for optical antennas as far as possible.

### 2.1. Impedance

The frequency-dependent complex conductivity of a material  $\tilde{\sigma}(\omega)$  relates the total local current density  $\mathbf{J}(\omega)$  as the

fundamental material response to the local electric field  $\mathbf{E}(\omega)$  as [1]

$$\mathbf{J}(\omega) = \tilde{\sigma}(\omega)\mathbf{E}(\omega). \quad (1)$$

This relationship is sometimes referred to as the microscopic form of Ohm's law.

The impedance  $Z$  of a homogeneous volume of length  $L$  and cross section  $A$  is linked to the intrinsic impedivity (i.e. complex resistivity) of the material  $\tilde{\rho}(\omega) = 1/\tilde{\sigma}(\omega)$  by

$$Z = \tilde{\rho} \frac{L}{A}. \quad (2)$$

Assuming a homogeneous current density normal to the cross section  $A$ , and an electric field oriented parallel to the length  $L$ , the current through the volume and voltage across the volume can be assigned as  $I = |\mathbf{J}|A$  and  $V = |\mathbf{E}|L$ , respectively. Combining these with equation (2), one recovers the well known macroscopic form of Ohm's law,  $Z = V/I$ .

The impedance  $Z$  is complex in general, the sum of the real resistance  $R$  and imaginary reactance  $X$ , both with units of ohms ( $\Omega$ ).  $Z$  is related to the material parameters of the conducting medium by [1, 67, 68]

$$Z = R - iX = \sqrt{\frac{\mu}{\epsilon}} = \sqrt{\frac{i\omega\mu}{i\omega\text{Re}(\epsilon) - \text{Re}(\tilde{\sigma})}}, \quad (3)$$

where  $\mu = \mu_0\mu_r$  and  $\epsilon = \epsilon_0\epsilon_r$  are the complex permeability and permittivity of the material, respectively<sup>1</sup>.

In circuits, impedance quantifies the extent to which current is inhibited through an electronic element. The resistance corresponds to temporally in-phase voltage and current, leading to real power loss (i.e. through heat). The reactance, on the other hand, is related to power stored in the electric or magnetic field.

More generally, any medium can be described in terms of its impedance using the right-hand side of equation (3). An alternative form in terms of electric and magnetic fields is the wave impedance defined at location  $r$  as

$$\eta = \mathbf{E}(r)/\mathbf{H}(r), \quad (4)$$

again measured in units of ohms ( $\Omega$ ).  $\eta$  is used instead of  $Z$  to indicate whether the impedance relates to the EM fields or the circuit bound voltage and current. Nevertheless, equations (3) and (4) are conceptually equivalent. At an interface where an EM wave penetrates into a medium, the surface impedance  $Z_S$  may be used [1].

The impedance of free space  $\eta_0$  is calculated from (3) as  $\eta_0 = 376.7 \Omega$  for a transverse electromagnetic (TEM) wave using the permittivity and permeability of vacuum,  $\epsilon_0 = 8.854 \times 10^{-12} \text{ F m}^{-1}$  and  $\mu_0 = 4.0\pi \times 10^{-7} \text{ H m}^{-1}$ , respectively. It is important to note that this impedance  $\eta_0$  is not applicable in regions where the electric field and magnetic field are out of phase, as in the near-field of an antenna or inside the medium (see section 2.5 for the definition of the

<sup>1</sup> In engineering, impedance is usually written as  $Z = R + jX$ . The opposite signs for the imaginary numbers  $i$  and  $j$  result from the different sense of rotation of the time-harmonic exponentials  $\exp\{-i\omega t\}$  and  $\exp\{j\omega t\}$  typically used in physics versus engineering, respectively.

near-field). In the near-field of an electrically short electric dipole, for example, the wave impedance<sup>2</sup> is complex and is associated with a greater value of  $|\mathbf{E}|/|\mathbf{H}|$  compared to free space [1, 6].

## 2.2. Input impedance in conventional antennas

In order to better understand the requirements and limitations of impedance matching in the optical regime, we first discuss impedance in a conventional sense, as it is understood for, e.g., RF antennas. It is well known that maximum power transfer between two circuits requires that their impedances be complex conjugates of each other at the junction [69]. The selection of circuit parameters to achieve this conjugate condition is called impedance matching. In traditional antenna design, impedance is characterized at the feed point of the antenna, where it makes a junction with the rest of the circuit. This input impedance is a critical antenna parameter defined as the ratio of voltage to current at the feed point:  $Z_{\text{in}} = V_{\text{in}}/I_{\text{in}} = R_A - iX_A$ . The real part of the antenna input impedance  $R_A$  can be broken into two components  $R_A = R_r + R_\Omega$ .  $R_r$  is the radiation resistance, responsible for power lost by radiation (or scattering, i.e., reradiation in the case of a receiving antenna), and  $R_\Omega$  is the loss resistance, responsible for power lost through Ohmic heat (i.e., absorbed power) [6–8].

As an example, figure 3 shows an antenna connected to a load via a transmission line in both cartoon (a) and circuit schematic (b) forms. An incident wave creates voltage  $V_T$  and current  $I_T$  on the antenna. Due to the transmission line characteristic impedance  $Z_0$ , the transmission line presents a modified load impedance  $Z'_L = V_{12}/I_T$  at the interface at terminals 1 and 2. Impedance matching occurs when  $Z'_L = Z_A^*$  (where the asterisk represents the complex conjugate). If the connection between the load and the transmission line is also impedance matched, the power delivered to the load by the antenna is maximum.

The antenna is a tool to convert electrical energy in the form of electric current or voltage into far-field propagating energy, or vice versa. That is, in a conventional sense, the antenna itself is a device to impedance match a circuit to free space. Poor impedance matching results in power reflections at the interface between circuit components, and correspondingly poor power transduction between them. In the case of a poor impedance match, the antenna will still transfer radiant energy to or from free space. For example, even the open terminal of an abruptly terminating waveguide such as a severed coaxial cable fed by a time-harmonic voltage source can emit radiation, albeit poorly.

## 2.3. Limit of delivered power

Even a perfectly impedance-matched antenna does not deliver all the energy available from the incident wave to the

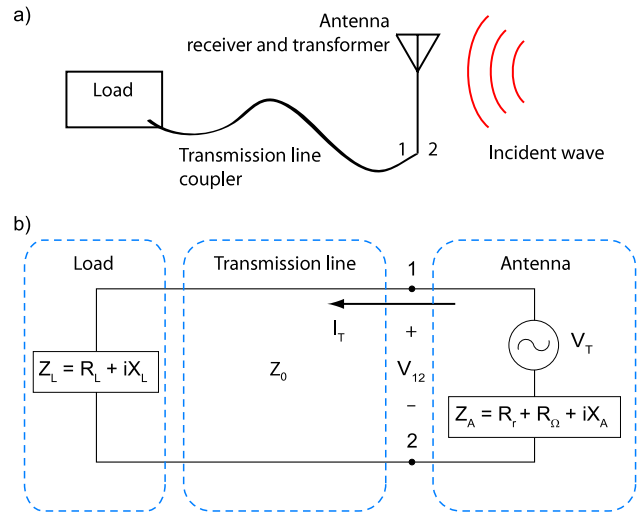


**Figure 3.** A load-coupled antenna illuminated by an incident wave in cartoon (a) and circuit schematic (b) forms. The wave produces voltage  $V_T$  on the antenna with impedance  $Z_A$ . The load impedance  $Z_L$  is transformed by the transmission line, becoming  $Z'_L$  at the junction at points 1 and 2. Impedance matching occurs when  $Z'_L = Z_A^*$ .

load. Impedance matching corresponds to maximum power transfer, but even in the ideal case, only half of the captured power is delivered to the load, and the rest is reradiated or lost as heat [6].

The power delivered to each resistive element ( $R_i$ ) in figure 3 is given by  $P_i = 0.5|I_T|^2 R_i$  with current  $I_T = V_T/[R_L + R_A - i(X_L + X_A)]$  [6]. This can be used to compare the power dissipated by the antenna,  $P_A = P_\Omega + P_r$ , to the power delivered to the load  $P_L$ . Figure 4 shows  $P_A$  and  $P_L$  normalized to the maximum load power as a function of  $R_L/R_A$ . When the load resistance is much lower than the antenna resistance, the power delivered to the load approaches zero, and all the power is lost as heat or reradiated. Conversely, if the load resistance is much higher than the antenna resistance, both  $P_A$  and  $P_L$  decrease because  $I_T$  decreases. It is interesting to note that with increased  $R_L/R_A$ ,  $P_A$  decreases faster than  $P_L$ . Thus if one wishes to minimize scattering ( $P_r$ ) or absorption ( $P_\Omega$ ) while still maintaining a substantial amount of load power (although not maximum), one could deliberately mismatch the impedances.

In general, the input impedance of the antenna  $Z_A$  depends on the geometry of the antenna, feed location, and mode of operation. The dependence of the input (circuit) impedance of an antenna on the antenna geometry, surrounding medium, and local electronic circuit environment has been the subject of intense study in RF engineering [6, 10, 70]. As a reference, the input impedance of a classical  $L = \lambda/2$  centre-fed thin (i.e.  $L \gg a$ , where  $a$  is the wire radius) wire antenna operating at the fundamental dipolar resonance, and isolated in vacuum is  $Z_A = 73.1 - i42.5 \Omega$ , as calculated analytically using the induced electromotive force (EMF) method (integration of the Poynting vector over the surface of the antenna), or numerically using the method of moments [6].

<sup>2</sup> In the near-field, it could be argued that the ratio of the electric to magnetic field should not be called wave impedance, since the near-field implies that the field is non-propagating. However, in the interest of consistent nomenclature, we retain this terminology.

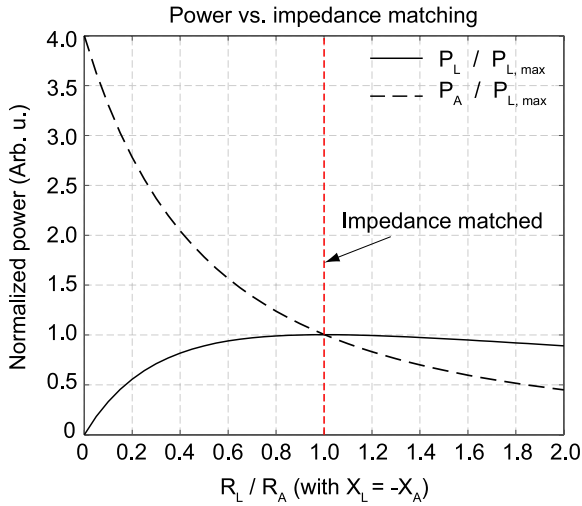


**Figure 4.** Power delivered to an antenna-coupled load,  $P_L$ , as a function of  $R_L/R_A$  with the constraint  $X_A = -X_L$ . Maximum power transfer to the load occurs when  $R_L/R_A = 1$ . Even when this condition is met, only half of the power is delivered to the load; the rest is absorbed or reradiated via  $P_A$ .

#### 2.4. Antenna resonance

With its simple geometry, the linear wire antenna often serves as a model for studying antenna properties. The resonant length tuning of the wire antenna has been studied in great depth [10, 70]. However, only for a very thin wire (radius  $a \ll \lambda$ ) or cylinder of infinite length does an exact analytical solution for associated current resonances and electromagnetic fields exist. For a cylinder of finite radius and length a solution may be readily calculated using iterative or matrix methods to solve Hallén's integral equation or Pocklington's integral equation, or using numerical (e.g. finite element) approaches [70, 71].

One can gain an often satisfactory semi-quantitative understanding of the antenna resonances using two approximations: first, the linear antenna can be approximated as an elongated prolate ellipsoid with eccentricity near unity. The second is perfect conduction,  $R_\Omega = 0 \Omega$ , an approximation used often at RF due to the very high conductivity of metals at low frequencies, an approximation that we shall see fails at optical frequencies. Under these approximations, one finds the familiar successive sinusoidal oscillatory resonant current modes of order  $p$  with  $p + 1$  nodes along the long axis of the ellipse. Resonance is achieved when the total length  $L \approx p\lambda/2$ , where  $\lambda$  is the wavelength of the EM wave, resulting in a large current magnitude.

For a thin centre-fed dipole with finite length  $L$ , oriented in  $\hat{z}$ , and with maximum current  $I_0$ , the current standing wave is approximated by a sinusoid, with forced nulls at the antenna end points, and forced continuity at the feed point, yielding a symmetric current distribution [6, 9, 70]  $I(z) = I_0 \sin[k(L/2 - |z|)]$  as shown in figure 5(a). While the current of actual antennas is not exactly sinusoidal, the correction is minor near resonance, and the sinusoidal approximation is appropriate for calculating the far-field and radiation resistance of thin linear antennas [10].

In order to derive the impedance, an antenna can be viewed as an  $RLC$  circuit. In a series  $RLC$  circuit, current resonance occurs when the series impedance  $Z$  is purely real (i.e.,  $X = 0 \Omega$ ) [69]. Indeed, at resonance, the inductive impedance of the antenna (due to the current in the wire arms) and the capacitive impedance (due to the distance between the oppositely charged wire arm electrodes) cancel. Therefore, the resonance depends sensitively on the antenna length  $L$ . Figure 5(b) shows the calculated radiated power  $P_{\text{rad}}$ , radiation resistance  $R_r$ , reactance  $X_r$  (referred to the location of the current maximum), and input resistance  $R_{\text{in}}$  (i.e., resistance at the feed point) as a function of wavelength-normalized antenna length for a thin perfectly conducting linear centre-fed wire antenna with a sinusoidal current distribution. The radiation resistance and reactance at the current maximum are calculated according to the solution for the impedance using the EMF method with the assumption of a sinusoidal current distribution as [6]

$$\begin{aligned} \frac{2\pi}{\eta} R_r &= C + \ln(kL) - C_i(kL) \\ &+ \frac{1}{2} \sin(kL) [S_i(2kL) - 2S_i(kL)] \\ &+ \frac{1}{2} \cos(kL) [C + \ln(kL/2)] \\ &+ C_i(2kL) - 2C_i(kL), \end{aligned} \quad (5)$$

and

$$\begin{aligned} \frac{4\pi}{\eta} X_r &= 2S_i(kL) + \cos(kL) [2S_i(kL) - S_i(2kL)] \\ &- \sin(kL) \left[ 2C_i(kL) - C_i(2kL) - C_i\left(\frac{2ka^2}{L}\right) \right] \end{aligned} \quad (6)$$

where  $C = 0.5772$  (Euler's constant) and  $C_i$  and  $S_i$  are the cosine and sine integrals.

As seen in figure 5(b), resonances of a thin wire antenna occur when the length  $L$  is near an integer multiple of  $\lambda/2$  (the exact value for the fundamental dipole resonance is  $L = 0.4857\lambda$  for  $a \ll \lambda$ ) [9]. Resonances near even integer multiples of  $\lambda/2$ , called open-circuit resonances, are difficult to drive in practice by feeding at the centre of the antenna due to the extremely high input resistance. Resonances at odd multiples of  $\lambda/2$  are called short-circuit resonances, because current flows into the antenna with very little resistance [72].

#### 2.5. Far- and near-field regions

The primary emphasis of RF antenna theory is on far-field function for applications such as communication and remote sensing. The load interaction in these cases can often be handled separately as a circuit problem. Optical antennas must couple to far-field light as well, but significant emphasis is also placed on the near-field where antenna-load and antenna-emitter interactions take place. Between these regions the characteristics of the field change significantly. The properties of these different field regions can most easily be illustrated by considering an infinitesimally small electric dipole.

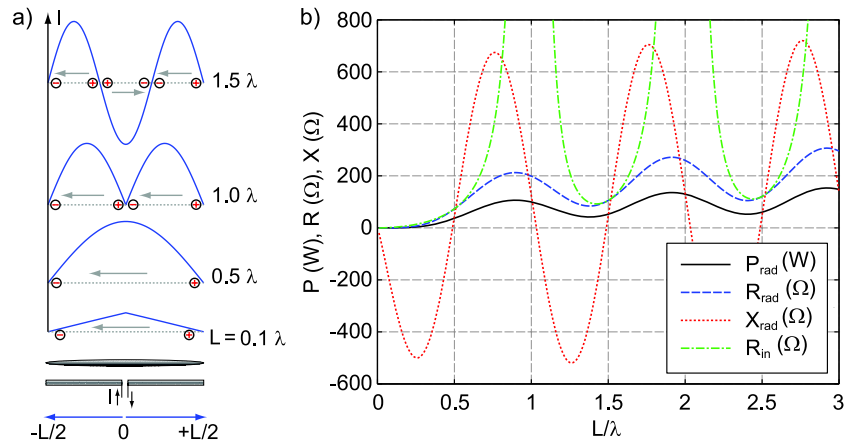


**Figure 5.** (a) Approximate sinusoidal current oscillations of centre-fed thin linear antennas of length  $L$ . (b) Radiated power  $P_{\text{rad}}$ , radiation resistance  $R_{\text{rad}}$ , reactance  $X_{\text{rad}}$  referred to the current maximum, and input resistance  $R_{\text{in}}$  (i.e. resistance at the central feed point) as a function of wavelength-normalized antenna length for a thin linear centre-fed wire antenna with a sinusoidal current distribution. Current resonances occur when  $X = 0$  (capacitive reactance cancels out inductive reactance, as in a series  $LC$  circuit), when the length is near multiples of  $\lambda/2$ .

Following [6], the solutions for the fields of an infinitesimal electric dipole antenna with length  $L \ll \lambda$ , a positionally invariant source current  $I_0$  (i.e. constant current along the length of the antenna), and wavevector  $k = \omega/c$  are

$$H_r = H_\theta = E_\phi = 0 \quad (7)$$

$$H_\phi = -i \frac{kI_0 L \sin \theta}{4\pi r} \left[ 1 + \frac{i}{kr} \right] e^{ikr} \quad (8)$$

$$E_r = \eta \frac{I_0 L \cos \theta}{2\pi r^2} \left[ 1 + \frac{i}{kr} \right] e^{ikr} \quad (9)$$

$$E_\theta = -i\eta \frac{kI_0 L \sin \theta}{4\pi r} \left[ 1 + \frac{i}{kr} - \frac{1}{(kr)^2} \right] e^{ikr}, \quad (10)$$

where  $r$ ,  $\theta$ , and  $\phi$  are the spherical coordinates associated with distance from the dipole, elevation angle, and azimuth angle, respectively, as shown in figure 6. Here the dipole itself is oriented in  $\theta = 0$ .

The character of the field changes with increased distance  $r$ , so the space around an antenna is conventionally broken into three field regions [6]. Nearest to the antenna is the reactive near-field. In this region, the reactive field dominates. This region extends to about  $r = 0.62\sqrt{D^3/\lambda}$ , where  $D$  is the largest dimension of the antenna. Beyond this is the radiating near-field (or Fresnel) region. In this region the radiative fields dominate, but there is still a substantial reactive component. The boundary of this region is  $r = 2D^2/\lambda$ . Beyond this is the far-field (or Fraunhofer) region. There the  $r^{-2}$  and  $r^{-3}$  terms are small, with the result that the  $1/r$  terms of the  $E_\theta$  and  $H_\phi$  components dominate. In this region the radiation pattern of the antenna is largely independent of distance and the electromagnetic field approximates a TEM plane wave.

## 2.6. The diffraction limit of far-field optics

One way to increase the energy density at the location of a load is by focusing incident radiation to the volume of the load. However, confinement of light to the desired

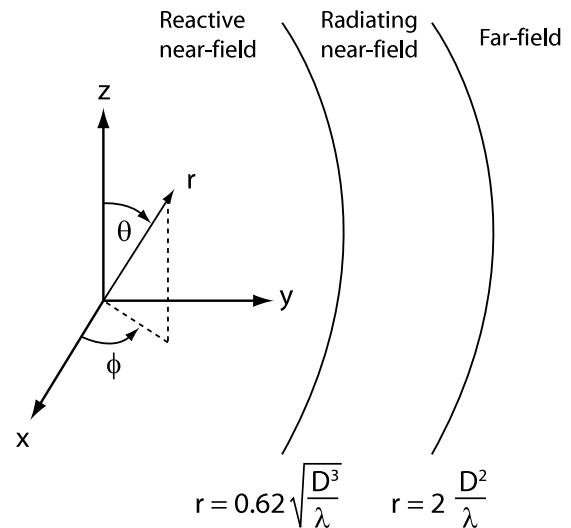


**Figure 6.** The space around an antenna is divided into three field regions with different field characteristics: the reactive near-field, radiating near-field, and far-field, in order of increasing distance from the antenna  $r$ . While RF antennas often operate in far-field applications such as communication and remote sensing, optical antennas often operate in the near-field.

nanometre dimensions for efficient interaction with quantum loads cannot be achieved with conventional far-field focusing optics. Spatial nanoconfinement of light requires near-field techniques to overcome the diffraction limit of far-field focusing. This can be understood by considering the spatial Fourier spectrum of a single point emitter located at the origin of a Cartesian coordinate system. For an infinitesimally small source the emission is composed of a continuum of all wavevector components  $k_x$ ,  $k_y$ , and  $k_z$ . The free-space propagating mode, however, can only sustain waves with a specific relationship between frequency and wavevector  $(2\pi\nu)/(2\pi/\lambda) = \omega/k = c$ , where  $\nu$ ,  $\lambda$ ,  $\omega$ , and  $c$  are the frequency, wavelength, angular frequency, and propagation

speed of the wave, respectively. Therefore, waves with spatial frequency components greater than the free-space wavevector  $k_x^2 + k_y^2 + k_z^2 > |\mathbf{k}|^2$  are evanescent and are attenuated quickly with distance; propagation acts as a low-pass frequency filter [68, 73]. Similarly, focusing a  $z$ -propagating wave to an arbitrarily small size would require arbitrarily high transverse spatial frequency components  $k_x$  and  $k_y$ , which are not available in far-field (i.e., propagating) light.

Furthermore, if the emitted light is collected by, e.g., an aperture or lens of diameter  $D = 2a$  at a distance  $R$  from the point source, then the  $k_x$  and  $k_y$  components are further reduced by the perimeter of the collection aperture. This gives rise to the well known diffraction limit. The Rayleigh criterion defines the minimum resolvable size scale in the far-field as

$$d \geq \frac{3.83}{\pi} \lambda \frac{R}{2a} \approx 1.22 \frac{\lambda}{2\text{NA}}, \quad (11)$$

where NA is the numerical aperture. In practice, using conventional optics the spatial resolution of an imaging system can be roughly estimated to about  $\lambda/2$ , e.g.  $\approx 200$  nm for blue light, and  $\approx 350$  nm for red light.

The general goal of optical antennas is to focus light to dimensions of a few nanometres not only for the purpose of ultrahigh spatial resolution imaging using near-field scanning probe techniques, but, as already indicated above, sub-diffraction-limited focusing is an essential concept of enhanced radiation transfer to a quantum load. Higher spatial resolution can be achieved by taking advantage of the evanescent wavevectors associated with high spatial frequency components of light before they evanescently decay. The region where these wavevector components still maintain a substantial magnitude is referred to as the optical near-field.

### 3. Metals at optical frequencies

One of the primary differences between conventional (RF) and optical antennas is the substantial increase in resistance in metals with decreasing wavelength beyond the millimetre regime. As mentioned above, RF antenna theory often implements an assumption of negligible Ohmic loss (compared to radiative loss) owing to the high DC conductivity. Optical antennas, however, are subject to significant and largely intrinsic Ohmic loss and a current phase offset with respect to the incident driving electric field, as described in this section.

#### 3.1. Drude–Sommerfeld free-electron model

Within the Drude–Sommerfeld free-electron model, noble metals are described as gases of noninteracting electrons with a frequency-dependent dielectric function. The dielectric function  $\epsilon_r(\omega)$  is derived by solving the equation of motion for the electrons driven by a time-harmonic electric field and introducing an empirical effective electron relaxation time  $\tau_D$  [1]. The solution is similar to that of a damped harmonic oscillator, but, with no restoring force, an intrinsic resonance

occurs at  $\omega = 0 \text{ s}^{-1}$  (the Drude peak) [74]. The resulting frequency dependence of  $\epsilon_r(\omega)$  is given by

$$\epsilon_r(\omega) = \epsilon_1(\omega) + i\epsilon_2(\omega) = 1 - \frac{\omega_p^2}{\omega^2 + i\gamma\omega}, \quad (12)$$

where  $\gamma = 1/\tau_D$  is the electron relaxation rate,  $\omega_p = (Ne^2/\epsilon_0 m^*)^{1/2}$  is the plasma frequency,  $N$  is the number of electrons per unit volume,  $e = 1.602 \times 10^{-19} \text{ C}$  is the electron charge,  $\epsilon_0 = 8.854 \times 10^{-12} \text{ F m}^{-1}$  is the permittivity of free space, and  $m^*$  is the effective mass of the electron, different from the rest mass  $m_e = 9.11 \times 10^{-31} \text{ kg}$ . As the mean free time between electron scattering events within the free-electron model, the relaxation time  $\tau_D$  parameterizes the cumulative effects of various electron scattering processes. The relaxation rate has contributions from electron–electron scattering, temperature-dependent electron–phonon scattering, scattering at grain boundaries, impurity and defect scattering, and surface roughness scattering contributions [75, 76]. However, the model does not include absorption via interband transitions. The parameters  $\gamma$  and  $\omega_p$  can be extracted from a fit to experimental data below the onset of interband transitions [77–79]. As an example for gold, resulting fit parameters are approximately  $\tau_D = 1/\gamma = 14 \pm 3 \text{ fs}$  and  $\hbar\omega_p = 8.48 \text{ eV}$ , though there can be significant variation depending on the measurement technique and sample properties [80]. The Drude model is purely phenomenological and does not provide physical insight into the damping mechanism (i.e., individual effects of sample thickness, surface roughness, volume fraction of crystal boundaries, impurities, electron–electron or electron–phonon scattering rate, or finite-size effects). It nevertheless describes the relationship between the permittivity and the collective electron damping in the low-frequency region dominated by the free-carrier response, and is thus sufficient for the purpose of understanding the main features of the frequency-dependent conductivity in the transition regime between RF and optical antennas.

#### 3.2. Conductivity at optical frequencies

In metals, the complex conductivity  $\tilde{\sigma}(\omega)$  is of particular importance as the real part defines Ohmic losses and the imaginary part is responsible for a phase offset between the local electric field and current density [1].  $\tilde{\sigma}(\omega)$  is related to the dielectric function as

$$\tilde{\sigma}(\omega) = \sigma_1 + i\sigma_2 = -i\epsilon_0\omega(\epsilon_r - 1). \quad (13)$$

Figure 7 shows the complex conductivity  $\tilde{\sigma}(\omega) = \sigma_1(\omega) + i\sigma_2(\omega)$  of the Drude–Sommerfeld free-electron model, real part (solid line) and imaginary part (dashed line), with  $\tau_D = 14 \text{ fs}$  and  $\hbar\omega_p = 8.48 \text{ eV}$  as found by a fit to experimental data for gold as a representative example, with similar behaviour for most metals with free valence electrons [80].

The frequency dependence of the conductivity allows for the assignment of four regimes with different material responses. Following [1], first is the long wavelength region (I,  $\lambda \gtrsim 1000 \mu\text{m}$ ) where RF antennas operate, called the Hagen–Rubens regime. It is associated with  $\sigma_1 \gg \sigma_2$ . In

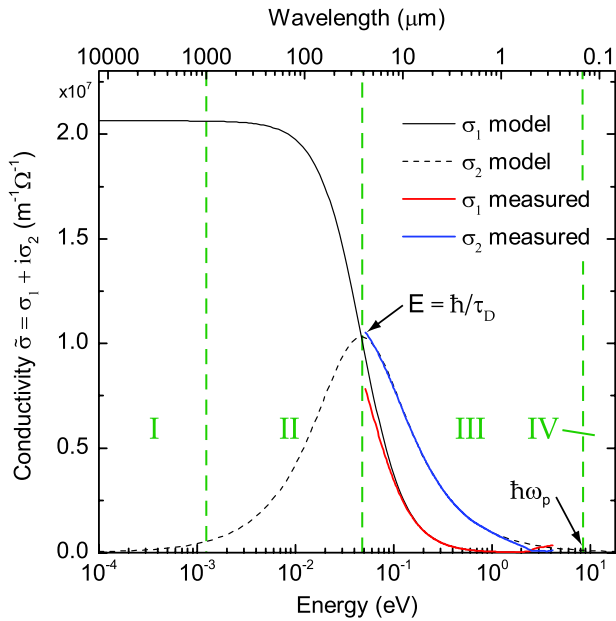


**Figure 7.** The complex conductivity of gold  $\tilde{\sigma}(\omega) = \sigma_1(\omega) + i\sigma_2(\omega)$  according to the Drude–Sommerfeld free-electron model, real part (solid line) and imaginary part (dashed line), with  $\tau_D = 14$  fs and  $\hbar\omega_p = 8.48$  eV. While RF antennas exhibit an extremely high real conductivity and low imaginary part (region I), optical antennas are subject to low real conductivity, leading to significant Ohmic loss (regions II and III). Region IV is the transparent regime where light has little effect on electron motion [1, 80].

this range, the response of the free electrons to an EM field is governed primarily by the DC conductivity. The electron motion is in phase with the electric field. Next in the far-IR is a transition regime (II), characterized by a decreasing  $\sigma_1$  and an increasing  $\sigma_2$ , with a crossover point at angular frequency  $E/\hbar = \gamma = 1/\tau_D$ , the relaxation rate. This defines the lower edge of the relaxation regime (III). This regime incorporates the mid- to near-IR spectral range. It is characterized by a significantly reduced real part and high imaginary part compared to the Hagen–Rubens regime, and is thus associated with greater Ohmic energy damping and a large phase offset between the excitation field and the charge motion. This region extends to the plasma frequency. For frequencies  $\omega > \omega_p$ , the electrons only weakly respond to the field oscillations, and light is able to pass through the medium. This region is therefore called the transparent regime (IV). Optical antennas operate in the second and third regions since the interaction between light and charge carriers is much lower in the transparent regime.

#### 4. Optical antenna resonances

Antenna resonances were described above in terms of standing current waves at RF. For optical antennas, resonances are understood in terms of bound surface waves instead. This physical difference is the main reason RF antenna design rules are challenging to scale to optical frequencies, but it is also responsible for the locally enhanced fields that make

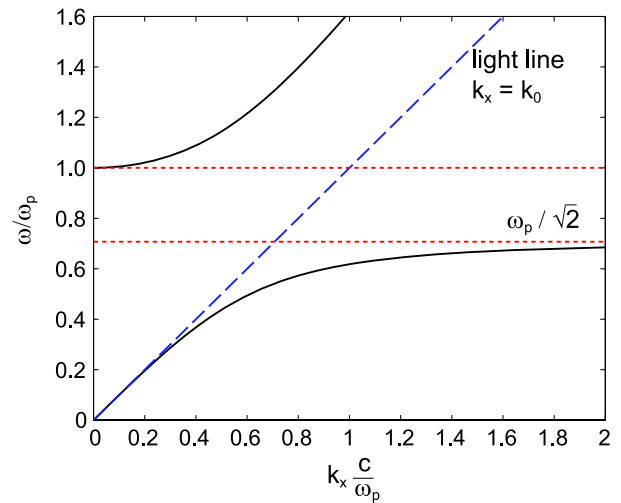


**Figure 8.** SPP dispersion at the interface of vacuum and a Drude metal (black solid line). At low frequencies, the SPP wavevector  $k_x$  is nearly equal to that of light indicated by the light line (blue dashed). At high frequencies the wavevector mismatch between the SPP and free-space light limits their interaction.

optical antennas useful for interactions with quantum loads. Antenna resonances define the properties of the receiver of the RTC system. The nature of these resonances and their characteristics are the subjects of this section.

##### 4.1. Surface plasmon polaritons

Electromagnetic boundary conditions at a metal–dielectric interface allow for a surface wave solution, called a surface plasmon polariton (SPP) [4]. SPPs are coherent charge oscillations at the interface between a metal and a dielectric, associated with a transverse magnetic (TM) surface wave [81–83]. For an SPP travelling in the  $x$ -direction at the interface between a metal ( $z < 0$ ) and a dielectric ( $z > 0$ ) with respective relative permittivities  $\epsilon_1$  and  $\epsilon_2$ , the dispersion relation is given as

$$k_x = k_0 \sqrt{\frac{\epsilon_1 \epsilon_2}{\epsilon_1 + \epsilon_2}}, \quad (14)$$

where  $k_0 = \omega/c_0$  is the wavevector in vacuum and  $c_0$  is the speed of light in vacuum.

Figure 8 shows the dispersion relation of an SPP at the interface between a Drude (free-electron) metal and vacuum, normalized by the plasma frequency  $\omega_p$  [1, 2]. At low (e.g., radio) frequencies,  $|\epsilon_1| \gg 1$ . The ratio under the square root in equation (14) therefore approaches unity, and the wavevector of the surface wave is nearly equal to that of the propagating wave governed by the light line  $k_x \approx k_0$ , allowing SPP interaction with free-space modes. However, at high (e.g., optical) frequencies (but below  $\omega_p$ ),  $k_x > k_0$ , so the SPP and propagating wave can interact only weakly, and the SPP is strongly bound to the surface. Various methods may be employed to overcome the momentum mismatch including increasing the index of refraction of the dielectric on one side of a metal film, or by making a grating at the interface [4, 39, 81].

#### 4.2. Spatial SPP behaviour

A nano-optical load can benefit from the concentrated EM energy in the SPP evanescent field. The spatial extent of the evanescent field of a SPP in the  $z$ -direction normal to the surface is governed by the imaginary  $k_z$  wavevector component. The characteristic length  $l_z$  gives the distance from the surface at which  $|E(z)|/|E(z=0)| = 1/e$ . For medium  $i$  (metal,  $i = 1$ ; dielectric,  $i = 2$ ), with complex dielectric function  $\epsilon_i = \epsilon'_i + i\epsilon''_i$ ,  $l_z$  is given by

$$l_{z,i} = \frac{1}{\text{Im}\{k_{z,i}\}} = \frac{\lambda}{2\pi} \left( \frac{\epsilon'_1 + \epsilon_2}{\epsilon_i^2} \right)^{1/2}. \quad (15)$$

Figure 9(a) shows the SPP normalized electric field magnitude along the  $z$  direction at a Drude metal/air interface for  $\lambda = 500, 750,$  and  $1000$  nm. Penetration into the air decreases with decreasing wavelength, illustrating the bounded nature of surface waves at higher frequencies compared to RF. The field penetration into the metal is also called the skin depth  $\delta$ . Notably, as shown in figure 9(b),  $\delta$  for gold, as calculated from experimental data, is largely wavelength independent throughout the near- to mid-IR range with  $\delta \sim 22$  nm [80]. In the visible, the skin depth of the Drude free-electron metal in (a) varies only slightly with frequency, in contrast to the measured skin depth for gold, which reaches  $\sim 45$  nm due to interband transitions.

Localized SPP resonances disappear when the resonator length exceeds the SPP propagation length [84]. The propagation length of a surface plasmon is given by [81]

$$L_{\text{spp}} = \frac{c}{\omega} \left( \frac{\epsilon'_1 + \epsilon_2}{\epsilon'_1 \epsilon_2} \right)^{3/2} \frac{\epsilon_1'^2}{\epsilon_1''}. \quad (16)$$

#### 4.3. Optical antenna as a cavity resonator

The connection between the modes of conventional RF and optical antennas has been investigated using a Fabry–Pérot or similar cavity model, with SPP reflection at the ends defined by a length-dependent reflection coefficient [85–87]. As expected, current resonances were found to occur when the length of the antenna was equivalent to an integer multiple of half the intra-cavity wavelength. Optical antenna resonances are distinguished from classical antenna resonances by applying a modified wavevector for the cavity compared to that for free space, related to the different material properties (i.e., frequency-dependent permittivity) and the typically lower aspect ratio of the antenna at optical frequencies. A greater ratio of the cavity wavevector to the free-space wavevector is associated with greater binding of the wave to the surface (i.e. a plasmonic wave), correspondingly lower radiated power, decreased resonant length, and the introduction of subradiant and superradiant modes as the antenna resonant length decreases below half the free-space wavelength. Thus the ideal classical antenna can be considered equivalent to a plasmonic antenna, but with a reflection coefficient of  $r = 1$  and with a cavity wavevector equal to the free-space wavevector [87]. Plasmonic antennas are characterized by SPP dispersion, which exhibits a greater wavevector on the structure surface compared to free space.

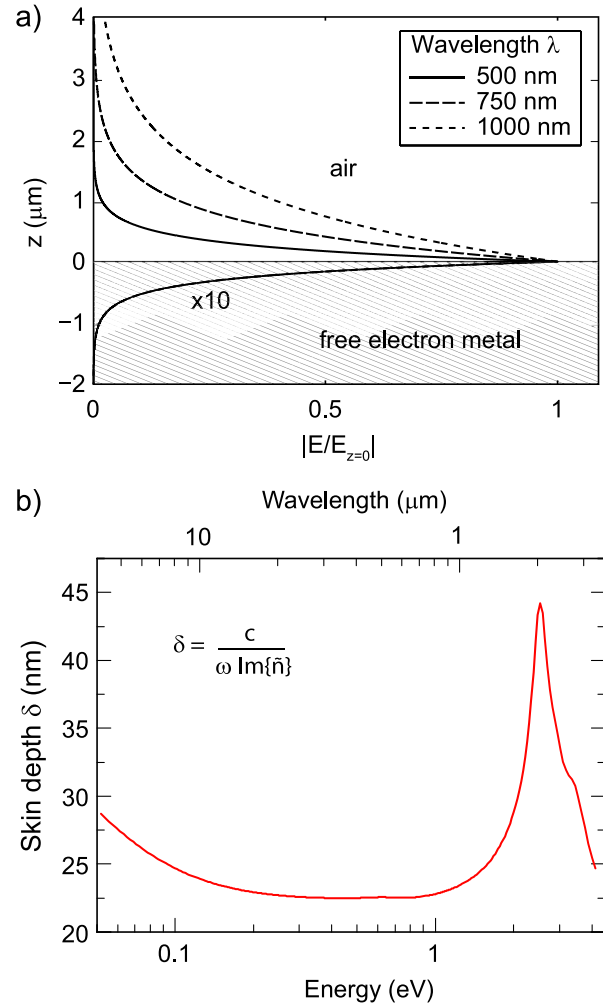


**Figure 9.** Evanescent electric field penetration into (a) a free-electron (Drude) metal and air supporting a surface plasmon polariton for  $\lambda = 500, 750,$  and  $1000$  nm. Longer wavelengths are associated with greater penetration into the air, while shorter wavelengths are bound more strongly to the interface. The field penetration into the air is much greater than the skin depth  $\delta$  of the metal shown in (b) as a function of energy for gold using measured data from [80].

#### 4.4. Effective wavelength scaling

RF theory predicts a fundamental dipolar resonance on a wire antenna for lengths near integer multiples of half the wavelength as discussed above [6]. However, at optical frequencies, the increased wavevector compared to that of free space is associated with an increased SPP effective mode index  $n_{\text{eff}}$  [86]. The result is a reduction of the resonant length compared to that expected from RF theory for a given excitation wavelength. According to finite element models, the resonant lengths for plasmonic rods occur near integer multiples of half of the SPP wavelength (or effective wavelength) instead of the free-space wavelength [86]. The relationship between the free-space wavelength  $\lambda_0$  and the antenna length  $L$  required to achieve resonance of order  $m$  is given as

$$\frac{m\lambda_{\text{eff}}}{2} = L(\lambda_0) + 2\psi(\lambda_0) \quad (17)$$

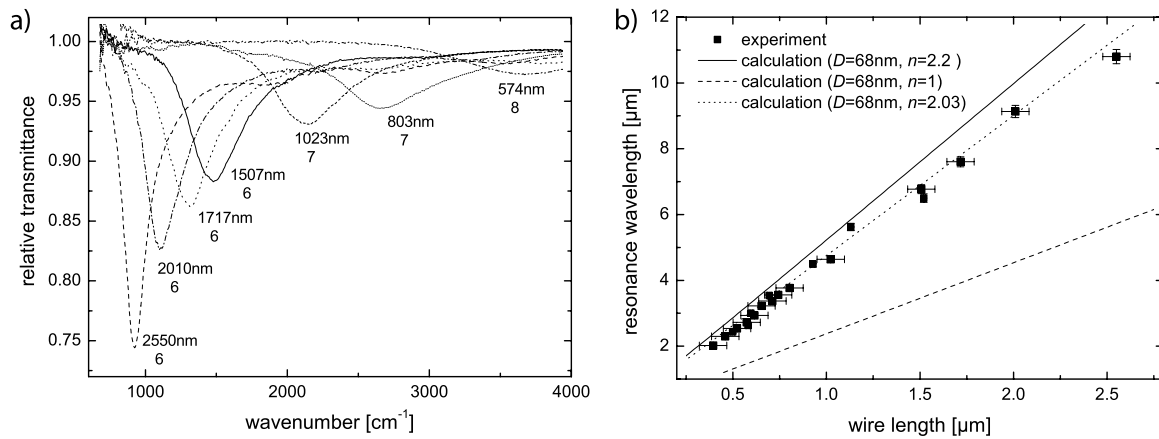


**Figure 10.** Infrared transmission spectra (a) and effective wavelength scaling (b) for gold linear optical antennas. The resonant antenna lengths are linearly related to the free-space wavelength. The numbers given for each minimum in (a) correspond to antenna length and the number of antennas included in each measurement. In (b) data are compared to the theoretical model of [88] with a single fit parameter  $n_{\text{eff}} = 2.03$  with antenna diameter  $D = 68$  nm. Adapted with permission from [94]. Copyright 2008 American Institute of Physics.

where  $\lambda_{\text{eff}} = \lambda_0/n_{\text{eff}}$  is the effective wavelength and  $\psi(\lambda_0)$  is an added length accounting for a phase shift upon reflection at the cavity terminals [18, 87]. The additional length is comparable to the  $1/e$  decay length in the wave transverse direction (as given by equation (15)). If  $L \gg \psi$ , equation (17) can be approximated to give  $\lambda_{\text{eff}} = 2L$  for the fundamental  $m = 1$  dipolar mode.

With the effective SPP mode index also dependent on the wire geometry, theoretical models have been developed directly linking the antenna geometry to the resonance wavelength [88, 89]. Models based on the extinction cross section as calculated using electrodynamics simulations based on the discrete dipole approximation verified the linear resonant length scaling and identified differences based on the type of metal used, especially for higher order resonances [90]. Investigations of the radius dependence of a plasmonic rod antenna show that decreasing the radius increases the effective mode index [91]. Hence, according to equation (17), decreasing the radius would require lengthening of the antenna to retain resonance for a given wavelength.

The linear scaling relationship of the resonant length with the effective wavelength has been verified experimentally using far-field spectroscopic measurements in the visible [92] and infrared [93–95]. Decreased resonant length compared to  $\lambda_0/2$  has been measured using nonlinear optics [96], thermal absorbers in the infrared [34], and near-field techniques [97–99]. Figure 10 shows the transmission spectra in the mid-infrared for gold linear wire antennas with lengths in the range  $L = 0.5\text{--}2.5$   $\mu\text{m}$  and width and height  $w \approx h \approx 60$  nm [94]. The rods were fabricated by electron beam lithography on a ZnSe substrate. The effective wavelength scaling is observed by selecting the wavelength of minimum transmission for each antenna length as shown in (b). The data were fitted to the effective wavelength model in [88] with good agreement with a single adjustable parameter  $n_{\text{eff}}$ . Resonant length scaling depends in general on the geometrical details of the antenna (diameter, cross section, surface roughness, etc.) and the material properties of the

surrounding medium. Typical values for  $n_{\text{eff}}$  have been measured in the range of 1.5–3.0 [34, 93, 94, 96–99].

## 5. Impedance of optical antennas

Next we turn to the specific theoretical description of impedance of optical antennas. Impedance is one of the most important antenna parameters in the RF. It plays an equally important role in the description of the antenna–load interaction at optical frequencies, as it governs the coupling between the antenna and mode transformer or the load of the RTC system. Depending on the geometry of the antenna–load system, the impedance can be modelled in two different ways.

The first method is analogous to the input impedance analysis of centre-fed RF antennas, with input impedance described at an antenna ‘feed gap’. This method is useful for multi-element antennas with defined gaps (though the antenna may not actually be fed at the gap). The corresponding theoretical approach [72, 100–105] has been used to help understand experimental results [99, 106] in terms of impedance and field enhancement. This method will be discussed in greater detail in this section.

The second approach can be used for antenna configurations that do not have a well defined gap. Antenna–load interactions in this case can be assigned through the modification of the local density of states by the antenna [61]. Impedance can be defined to describe this interaction and provide a means for impedance matching. These types of antenna configuration will be discussed in further detail in section 6.7.

### 5.1. Gap excitation

Impedance analysis of gap excited and gap loaded optical antennas is similar to that of conventional RF antennas. The input impedance is defined at the antenna gap terminals as the ratio of the driving voltage to the displacement current through the gap [100]. The intrinsic antenna (self-) impedance

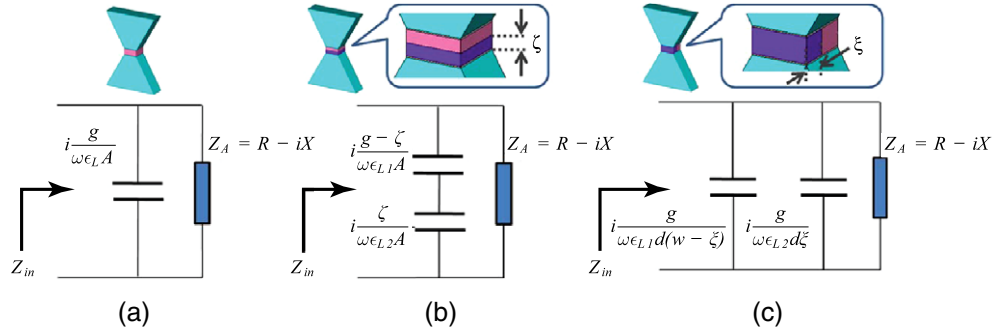


**Figure 11.** Circuit diagrams for optical antennas loaded with single (a), in-series (b), or in-parallel (c) nanoloads. The input impedance defined at the gap terminals is the parallel combination of the nanoload and the antenna intrinsic impedance  $Z_A$ . Adapted with permission from [105]. Copyright 2011 Optical Society of America.

is  $Z_A = R - iX$ , where  $R$  is the resistance and  $X$  is the reactance of the antenna.

A load positioned in the gap can be defined as a capacitor in parallel with the antenna intrinsic impedance. The impedance of the load is given by

$$Z_L = \frac{ig}{\omega\epsilon_L A} \quad (18)$$

where  $g$  is the length of the gap,  $A = wd$  is the cross sectional area of the gap, and  $\epsilon_L$  is the dielectric function of the load material [105]. Complex loads made of two or more materials can be modelled by assigning the load dimensions as appropriate fractions of the gap dimensions. Circuit representations for single loads, series loads, and parallel loads are shown in figures 11(a)–(c), respectively. For stacked loads (see figure 11(b)) one should replace  $g$  with the load thickness  $\zeta$  or  $g - \zeta$  in equation (18). For side-by-side loads (see figure 11(c)), one should replace width  $w$  with  $\xi$  or  $w - \xi$ .

The intrinsic input impedance can be determined by inserting a load with  $\epsilon_L = \epsilon_s$  where  $\epsilon_s$  is the dielectric function of the surrounding medium. In this case, the impedance is given by

$$Z_{in} = \frac{1}{\frac{1}{R - iX} - i\omega C}, \quad (19)$$

where  $C = \epsilon_s A/g$ . The real and imaginary parts of  $Z_{in}$  are

$$r_0 = \frac{R}{1 - 2CX\omega + C^2R^2\omega + C^2X^2\omega}, \quad \text{and} \quad (20)$$

$$x_0 = \frac{X - CR^2\omega - CX^2\omega}{1 - 2CX\omega + C^2R^2\omega + C^2X^2\omega}. \quad (21)$$

When loaded, the capacitance becomes  $C_L = \epsilon_L A/g$ . The input impedance with the load is determined by replacing  $C$  with  $C_L$  in equations (20) and (21). This model also produces an estimate of the frequency of the first open-circuit resonance corresponding to resonant scattering, given by [105]

$$\omega_0 = \frac{gX}{A(R^2 + X^2)\epsilon_L}. \quad (22)$$

Using this model, the input impedance of a dimer optical nanoantenna can be compared to the input impedance as

calculated using RF theory. For an antenna of length  $L = 110$  nm, radius  $a = 5$  nm, and gap size  $g = 3$  nm, the fundamental dipolar resonance ( $X_{in} = 0 \Omega$ ) occurs at  $f = 266$  THz ( $\lambda = 1.13 \mu\text{m}$ ) with  $Z_{in}$  of  $22 \Omega$ . In comparison, the radiation resistance of this geometry has also been calculated from the current density  $\mathbf{j} = -i\omega\epsilon_0[\epsilon(\omega) - 1]\mathbf{E}$  and total emitted power with the local electric field calculated numerically using the semi-analytical multiple-multipole (MMP) method [88]. For both gold and aluminum half-wave antennas with length  $L = 110$  nm and radius  $a = 5$  nm, the radiation resistance determined in this manner is  $R_r \approx 3 \Omega$ , suggesting that the Ohmic loss resistance for this geometry is  $R_\Omega \approx 19 \Omega$ . This is significantly less than the classical thin wire antenna  $Z_{in}$  of  $68.5 \Omega$  as calculated using the induced EMF method [6]. In comparison, a centre-fed single-walled nanotube antenna was found to have an extremely low radiation resistance of about  $0.04 \Omega$ , and a comparatively high input resistance of about  $100 \text{ k}\Omega$  due to significant absorptive loss [107].

## 5.2. Resonance tuning by loading

A load placed in the gap between two linear antenna segments has been shown to modify the resonance of the antenna-load system, both theoretically [100] and experimentally [108]. Inserting loads of higher permittivity results in increased gap capacitance and lower resonance frequencies for the antenna-load system. As an example, simulations of spherical silver nanoparticle dimers of total length  $L = 100$  nm, separated by a gap of  $g = 3$  nm, driven from a source with impedance  $10 \text{ k}\Omega$ , and loaded at the gap by either vacuum ( $\epsilon = \epsilon_0$ ),  $\text{Si}_3\text{N}_4$  ( $\epsilon = 4.1\epsilon_0$ ) or Si ( $\epsilon = 13.37\epsilon_0$ ) result in second order (open circuit) resonances of 665 THz, 605 THz, and 455 THz (450 nm, 500 nm, and 660 nm), respectively [72]. A very small gap width can be created in practice by, for example, using few-layer molecular spacer layers between template-grown nanorods [109] or implementing a slightly modified stacked antenna geometry, lithographically defining the metal elements with an overlap near the centre where dielectric material of only a few nanometres can be deposited between the metal layers [110]. However, when implementing these nanodisc materials with a

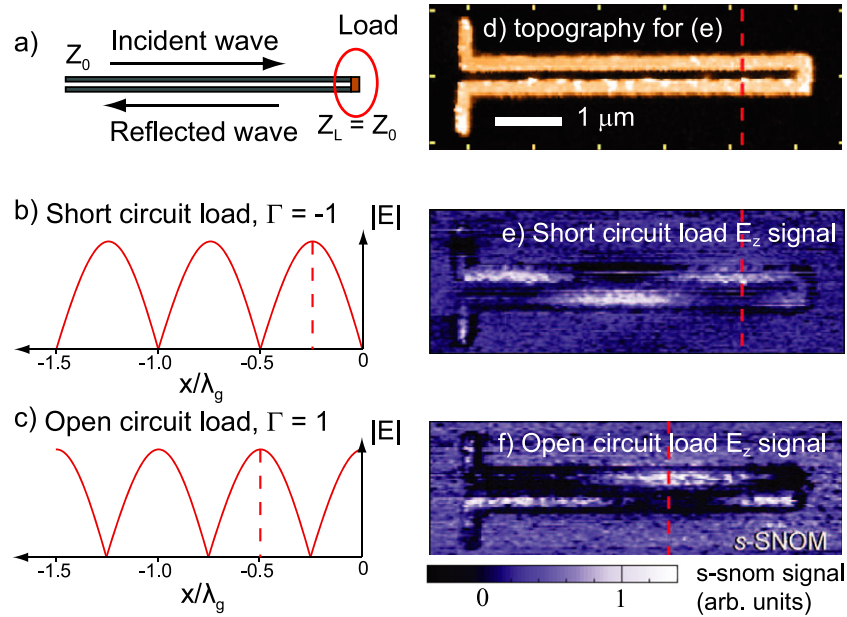


**Figure 12.** Standing waves (a) develop on a transmission line when the load presents an impedance different from the characteristic impedance of the line, resulting in reflection with reflection coefficient  $\Gamma$  related to the impedance mismatch. The two limiting values for the load are a short-circuit load  $Z_L = 0 \Omega$  (b) and an open load  $Z_L = \infty \Omega$  (c). The electric field magnitude at  $x = 0$  is either a null (for the short circuit) or a maximum (for the open). (d) The topography and sample normal electric field  $E_z$  as measured by s-SNOM for the short load (e) and open load (f). Reprinted with permission from [43]. Copyright 2010 Optical Society of America.

geometric scale of only a few nanometres, one has to consider that quantum finite-size effects become significant and fundamentally change the optical and electronic properties compared to those of the bulk material.

Instead of changing the material of the nanoload disc, varying its radius also affects the impedance and thus the resonance. Decreasing the radius of the nanoload increases its impedance according to equation (19). This has been verified experimentally using near-field measurements to characterize the amplitude and phase of a cylindrical dimer antenna with a connecting metal bridge [99]. For a full bridge radius equal to the antenna arm radius, a fundamental dipolar resonance was observed associated with the entire length of the connected dimer. As the radius of the bridge was reduced to  $a = 0$ , the resonance behaviour gradually shifted to that of two separate dipoles.

Immersing antenna dimers in an anisotropic liquid crystal dielectric load medium provides a way to control the electrical interaction between the two elements [103, 108]. Using electrodes near the antennas to control the orientation of the liquid crystal, one can tune the resonance frequency and polarization response of the dimers. Loading antennas with nonlinear materials has been suggested as a way to achieve optical memories, switches, and transistors using nanoantennas [104]. Active control of the antenna resonances might be achieved by using semiconductor loads which allow for optical control of the free-carrier density via optical pumping [111].

### 5.3. Measuring impedance matching with coplanar striplines

Theoretical investigations of the impedance of nanoloads are helpful in estimating the required antenna properties

for impedance matching. However, in order to design a fully integrated circuit consisting of antennas, loads, and transmission lines, one must be able to experimentally quantify the impedance of the load.

The degree of impedance matching, e.g., between two separate circuit elements connected by a coplanar two-wire transmission line, can be inferred from the standing wave pattern on the line [40]. A coplanar strip line consists of two parallel metal stripes on a substrate that together support voltage  $V$  and current  $I$  wave propagation with travelling wave solutions along  $x$  of [8]

$$V(x) = V_0 (e^{-\gamma x} + \Gamma e^{\gamma x}), \quad \text{and} \quad (23)$$

$$I(x) = \frac{V_0}{Z_0} (e^{-\gamma x} - \Gamma e^{\gamma x}), \quad (24)$$

with the characteristic impedance of the line  $Z_0$  related to the distributed load per unit length, and the complex propagation constant  $\gamma = \alpha + i\beta$  where  $\beta = 2\pi/\lambda_g$  and  $\lambda_g$  is the wavelength of the standing wave on the line.  $\Gamma$  is the reflection coefficient of the wave at the junction between the transmission line and the load. It is related to  $Z_0$  and the terminating load impedance  $Z_L$  (see figure 12) as

$$\Gamma = \frac{Z_L - Z_0}{Z_L + Z_0} = \Gamma_0 e^{i\theta}. \quad (25)$$

If the load is matched to the line,  $Z_0 = Z_L$ , and  $\Gamma = 0$  (i.e., there is no reflection). The limiting cases for the terminating load impedance are the short circuit ( $Z_L = 0 \Omega$ ) and the open circuit ( $Z_L = \infty \Omega$ ), resulting in reflections with  $\Gamma = -1$  and  $\Gamma = 1$ , respectively. Figures 12(a)–(c) show a conceptual view of standing wave generation on the

transmission line with wave reflection at the junction between the transmission line and the load. For a short-circuit load (b), the reflection coefficient is real  $\Gamma = -1$  and the wave has an amplitude of  $|E| = 0 \text{ V m}^{-1}$  at the location of the load. In contrast, the open load (the two striplines are disconnected) supports the maximum electric field magnitude, and the null occurs at a distance  $\lambda_g/4$  from the load.

As a verification of this theory at optical frequencies, scattering-type scanning near-field optical microscopy (s-SNOM) was used to measure the standing wave patterns on antenna-coupled coplanar striplines loaded by either a short or an open connection, finding good agreement with transmission line theory [43]. Figures 12(d)–(f) show the topography (d), and sample normal electric field  $E_z$  as measured by s-SNOM for the short load (e) and open load (f).

The impedance of an arbitrary load with respect to  $Z_0$  of a low-loss transmission line can in principle be quantified through the reflection coefficient [8]. The magnitude of the reflection coefficient can be calculated as

$$|\Gamma| = \frac{S - 1}{S + 1} \quad (26)$$

where  $S = V_{\max}/V_{\min}$  is the standing wave ratio, defined as the ratio of maximum to minimum voltage on the transmission line. At optical frequencies, the magnitude of the experimentally measured electric near-field can be used instead [40, 43]. The phase of the reflection coefficient is found by locating the first null in the voltage standing wave, at position  $x'$ , with

$$x' = \frac{\theta\lambda}{4\pi}. \quad (27)$$

A similar way to create optical interconnects for wireless optical broadcasting has been proposed [112]. This includes a circuit consisting of two waveguide-coupled antennas, one serving as a transmitter and the other as a receiver in the far-field. The antennas are impedance matched to the stripline by placing a load in the gap between the antenna elements. Even with radiation losses, the overall signal loss of the antenna transmission system is predicted to be significantly less than the loss if the air link were replaced by a continuation of the plasmonic waveguide.

Impedance matching was implemented experimentally with a single-wire plasmonic transmission line coupled to a bowtie antenna as a load [113]. Using numerical simulation, the antenna dimensions associated with the reflection coefficient minimum at the load (i.e., best impedance match) were found to be equivalent to those for the isolated antenna as determined via a parametric experimental study. Impedance matching in this configuration was checked using numerical techniques to calculate the complex characteristic impedance of the wire as  $Z_0 = 138 + i3.2 \Omega$  for free-space wavelength  $\lambda_0 = 672 \text{ nm}$ . This value is in good comparison with  $Z_0 = 216 + i5.5 \Omega$  as found by a different simulation for a coplanar strip transmission line [40].

These efforts provide the first steps towards antenna integrated optical circuitry. Future experimental and theoretical work should focus on verifying the accuracy of the

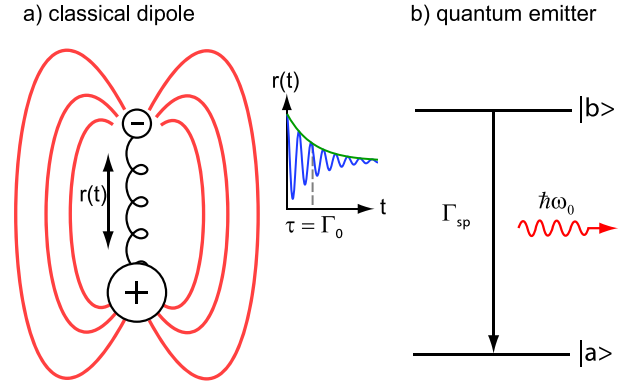


**Figure 13.** Classical and quantum emitters. (a) Classical radiating dipole modelled as an electron on a spring connected to an immobile atom core. The electron's oscillatory motion decays with time constant  $\tau = \Gamma_0$ . (b) A quantum emitter decays from energy  $|b\rangle$  to  $|a\rangle$  with rate  $\Gamma_{sp}$ , emitting a photon with energy  $E = \hbar\omega_0$ .

theory of the optical interconnect, investigating different types of transmission line, and systematic measurements of the impedances of different types of load including photodetectors [31], metal–oxide–metal (MOM) diodes [33, 114], and quantum loads, for example.

## 6. Optical antennas for emission

We now turn the discussion specifically towards antennas operating in the optical regime. In particular, we discuss the emission properties of optical antennas and antenna–emitter systems including classical and quantum emitters, radiative and nonradiative decay rates, and antenna–emitter interactions.

### 6.1. Emission of radiation from a classical dipole

The oscillating electric dipole could be considered as the most fundamental antenna. Consider the simple model of an electron with position  $\mathbf{r}(t)$  oscillating about an equilibrium position, bound to a stationary atom core as shown in figure 13(a). The periodic motion at small amplitudes experienced by the electron upon EM excitation can be modelled as a damped harmonic oscillator. Following [73] and [115], the equation of motion for the undriven radiating oscillator can be written as

$$m \frac{d^2 \mathbf{r}}{dt^2} + \omega_0^2 m \mathbf{r} = \mathbf{F}_r, \quad (28)$$

where  $\mathbf{F}_r$  is a reaction force experienced by the electron, corresponding to the loss of mechanical energy due to radiation of electromagnetic energy. In this model, this term accounts for all energy lost via radiation.  $\mathbf{F}_r$  is given by the Abraham–Lorentz formula

$$\mathbf{F}_r = \frac{q^2}{6\pi\epsilon_0 c^3} \frac{d^3 \mathbf{r}}{dt^3}. \quad (29)$$

Taking the solution for the charge motion to be of the form  $\mathbf{r}(t) = \mathbf{r}_0 \exp\{-i\omega_0 t\}$ , equation (29) can be rewritten using

$d^3\mathbf{r}/dt^3 = -\omega_0^2 \cdot d\mathbf{r}/dt$ . The equation of motion then takes the form

$$\frac{d^2\mathbf{r}}{dt^2} + \Gamma_0 \frac{d\mathbf{r}}{dt} + \omega_0^2 \mathbf{r} = 0, \quad \text{with} \quad (30)$$

$$\Gamma_0 = \frac{q^2 \omega_0^2}{6\pi \epsilon_0 m c^3} \quad (31)$$

where  $\Gamma_0$  is the rate of radiative damping of the electron motion. The relaxation lifetime of the oscillation (i.e., the time when the oscillation amplitude is a factor of  $1/e$  smaller than the initial amplitude) is  $\tau = 1/\Gamma_0$  with a typical value of  $\approx 20$  ns at optical frequencies (here, e.g.,  $\hbar\omega_0 = 2$  eV).

Now let us consider the system driven by an external electric field polarized in the direction of the dipole  $\mathbf{E}(t) = \text{Re}\{E_0 \hat{z} \exp^{-i\omega t}\}$ . The solution for the equation of forced motion is

$$\mathbf{r}(\omega) = \frac{-eE_0 \hat{z}}{m} \frac{1}{\omega_0^2 - \omega^2 - i\Gamma_0 \omega} \quad (32)$$

where  $e$  is the fundamental charge.  $\mathbf{r}(\omega)$  is a Lorentzian oscillator with resonance when  $\omega = \omega_0$ .

## 6.2. The atom as an antenna

Atomic radiation in the visible spectrum is well understood. The bright yellow light of a sodium vapour lamp is due to the  $3p \rightarrow 3s$  atomic transition with doublet transition wavelengths of  $\lambda = c/E = 589.0$  and  $589.6$  nm [116]. Since it is responsible for the radiation of electromagnetic waves, can the atom then be considered an optical antenna?

Let us consider a nondegenerate two-level quantum system with ground and excited states  $|a\rangle$  and  $|b\rangle$  (see figure 13(b)), and transition dipole moment operator  $\hat{\boldsymbol{\mu}}$ . This system decays from the excited state spontaneously with rate [73, 115]

$$\Gamma_{\text{sp}} = \frac{\pi \omega_0}{3\epsilon_0 \hbar} |\langle a | \hat{\boldsymbol{\mu}} | b \rangle|^2 \rho_{\mu}(\mathbf{r}_0, \omega_0), \quad (33)$$

where  $\epsilon_0$  is the vacuum permittivity,  $h = \hbar/(2\pi)$  is Planck's constant,  $E_b - E_a = \hbar\omega_0$  is the energy of the transition, and  $\rho_{\mu}$  is the partial local density of states (LDOS) at the location  $\mathbf{r}_0$  of the system. In vacuum, the electromagnetic density of states  $\rho_{\mu} = \rho_v$  is given by

$$\rho_v(\omega) = \frac{\omega_0^2}{\pi^2 c^3}. \quad (34)$$

Inserting equation (34) into (33), and introducing  $\boldsymbol{\mu}_{ba}^2 = |\langle a | \hat{\boldsymbol{\mu}} | b \rangle|^2$ , the spontaneous emission rate becomes

$$\Gamma_{\text{sp}} = \frac{\omega_0^3}{3\pi \epsilon_0 \hbar c^3} \boldsymbol{\mu}_{ba}^2. \quad (35)$$

We can now compare the radiative rates of the classical system and the quantum system. Taking the ratio of the quantum rate to the classical rate, we find that it is equivalent to the oscillator strength of the transition between two quantum levels, a dimensionless quantity given by [115]

$$f_{ab} = \frac{\Gamma_{\text{sp}}}{\Gamma_0} = \frac{2m\omega_0 \boldsymbol{\mu}_{ba}^2}{\hbar}. \quad (36)$$

For a one-electron atom, the oscillator strength for the transition between the ground state and the first excited state is  $\sim 1$ . Thus in the weak perturbation regime the classical description can be applied to describe the radiation of a quantum system to a good approximation. In fact, the radiative rate of the classical dipole emitter serves as an upper limit for the atomic rate of spontaneous emission [115]. With the classical dipole serving as an elementary antenna, the good agreement between the classical and quantum dipole models suggests that we can draw a close analogy between the radiative emission and absorption of a quantum system and classical antennas. This notion will be expanded on below in the formulation of the impedance of an atom [61].

Using equation (35) one can estimate the decay time of a nondegenerate two-level atom. Taking  $\boldsymbol{\mu}_{ba} = q^2 r_{21}^2$  as (one-electron charge)  $\times (1 \text{ \AA})$  (or  $1.602 \times 10^{-29}$  C m), and  $\omega_0 = 2 \text{ eV}/\hbar_{eV} = 3.04 \times 10^{15} \text{ rad s}^{-1}$ , the spontaneous decay rate is calculated using equation (35) as  $\Gamma_{\text{sp}} = 3.03 \times 10^7 \text{ s}^{-1}$ . The corresponding excited state lifetime is  $\tau = 1/\Gamma_{\text{sp}} = 33$  ns. In comparison, the measured lifetime of the transition from the  $4s4p^1P_1$  configuration of calcium to the lower energy  $4s^2^1S_0$  configuration ( $\omega_0 = 4.5 \times 10^{15} \text{ rad s}^{-1}$ ) is 4.5 ns with  $\boldsymbol{\mu}_{ba} = 2.4 \times 10^{-29}$  C m [117]. In general, typical radiative lifetimes of atomic transitions are of the order of a few nanoseconds [74, 118].

With  $\lambda_0 = 2\pi c/\omega_0$ , the decay rate takes on the alternative form

$$\Gamma_{\text{sp}} = \frac{8e^2 \pi^2}{3\epsilon_0 \hbar} \left(\frac{r}{\lambda_0}\right)^2 \frac{1}{\lambda_0}. \quad (37)$$

This form highlights the size mismatch  $r/\lambda_0$  inherent in the atom-field interaction. This size mismatch and the related long radiative lifetime of the excited state are indicative of the large impedance mismatch that the atom faces with free space. Comparing to the RF antenna discussion above, the atom has a low  $P_{\text{rad}}$ , but it cannot lose energy nonradiatively since  $R_{\Omega} = 0 \Omega$ . Either increasing the size of the system or decreasing the wavelength would increase the coupling to free space. However, these parameters are typically constrained. An alternative way to increase the coupling would be by increasing the energy density or local density of electromagnetic states as indicated by (33). This is where optical antennas come into play. Before discussing antenna-emitter interactions, however, we first discuss the radiative rate of the antenna itself.

## 6.3. Metallic resonators: radiative dephasing

One of the roles of an optical antenna is to control or enhance the radiative emission of a quantum emitter. For this to occur, the antenna must radiate efficiently, and with a faster rate than the quantum emitter. On the other hand, an antenna designed to feed energy into a load would benefit from a low total decay rate, making the energy available to the load via the near-field for a longer duration. In both cases it is important to understand the decay rate of optical antennas.

We first consider a metal sphere of radius  $a \ll \lambda$  in the quasistatic approximation with dielectric function  $\epsilon = \epsilon' + i\epsilon''$

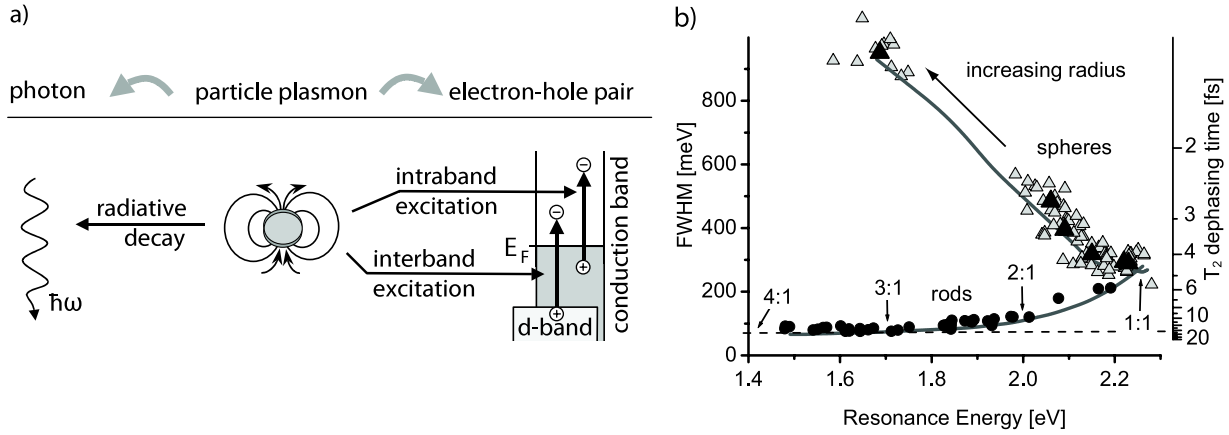


**Figure 14.** Energy damping in plasmonic particles. (a) Diagram showing the decay pathways for a particle plasmon: radiative decay resulting in a photon, and nonradiative decay via inter- or intraband excitation resulting in an electron-hole pair. (b) Measured linewidths of plasmon resonances for nanorods (circles) of different aspect ratios and nanospheres (open triangles) versus resonance energy. The corresponding  $T_2$  dephasing times are shown on the right-hand scale. The grey lines correspond to Mie theory (spheres) and a quasistatic calculation (rods). Adapted with permission from [54]. Copyright 2002 by the American Physical Society.

embedded in a medium with  $\epsilon_m$ . The induced dipole moment of the sphere is related to the incident electric field  $E_0$  as [4]

$$\mathbf{p} = \epsilon_0 \epsilon_m \alpha \mathbf{E}_0, \quad (38)$$

where the polarizability of the particle is given by

$$\alpha(\omega) = 4\pi a^3 \frac{\epsilon(\omega) - \epsilon_m(\omega)}{\epsilon(\omega) + 2\epsilon_m(\omega)}. \quad (39)$$

The Fröhlich resonance condition  $\epsilon' = -2\epsilon_m$  for the sphere is associated with a confined collective charge density oscillation termed a local surface plasmon polariton. This resonant behaviour is distinct from the conventional antenna resonance discussed above for several reasons. First, it is sensitive to the precise behaviour of  $\epsilon(\omega)$ . Notably, this can have great implications in field enhanced spectroscopy, for example, where the Raman scattering enhancement near such a particle scales with  $(\epsilon - \epsilon_m)/(\epsilon + 2\epsilon_m)$  to the fourth power [119]. Also, with the cycle period less than the average Drude electron scattering time  $1/\gamma$  as discussed above, coherent and superradiant behaviour arises, which may partially overcome limitations in radiative efficiency brought on by higher Ohmic loss at optical frequencies.

This quasistatic model, however, does not account for radiative energy losses that become significant with larger particle sizes. Generally, both radiative and nonradiative decay channels should be considered, as they define the efficiency of the transformation function of the RTC scheme. The total damping rate of an excited particle plasmon is given by

$$\Gamma = \Gamma_r + \Gamma_{nr}, \quad (40)$$

where  $\Gamma_r$  is the radiative decay rate and  $\Gamma_{nr}$  is the nonradiative rate. This is analogous to the RF antenna where the antenna resistance  $R_A$  has radiative  $R_r$  and nonradiative Ohmic  $R_\Omega$  contributions. As shown in figure 14(a) for a particle plasmon, radiative relaxation results in the emission of a photon, while nonradiative relaxation results in either an intra- or interband

excitation [54]. If nonradiative decay in the antenna dominates the total damping, then the antenna will be a weak emitter.

Compared to the atomic oscillators described in section 6.2 above, the much larger metallic particles have been found to exhibit significantly shorter radiative lifetimes. The scattering spectra of individual gold plasmonic nanoparticles of different sizes and shapes were systematically measured [54]. With  $\Gamma$  equal to the homogeneous linewidth of the scattering spectrum of an individual particle, the total dephasing time was determined using  $T_2 = 2\hbar/\Gamma$ . Figure 14(b) shows the measured linewidths  $\Gamma$  of plasmon resonances for nanospheres (open triangles) and nanorods of different aspect ratios (circles) versus resonance energy. The corresponding total (radiative and nonradiative)  $T_2$  dephasing times are shown on the scale on the right. The experimental measurements agree with Mie theory (for the spheres) and a quasistatic calculation (for the nanorods) as shown by the grey lines.

The dephasing time  $T_2$  is composed of radiative  $T_r$  and nonradiative  $T_{nr}$  components as

$$\frac{1}{T_2} = \frac{1}{T_r} + \frac{1}{T_{nr}}. \quad (41)$$

The  $T_2$  time for a nanorod with a 3:1 aspect ratio was measured to be  $T_2 = 16$  fs. From this value dephasing times of  $T_r = 160$  fs and  $T_{nr} = 18$  fs were estimated, indicating that the population decay time for these geometries is dominated by nonradiative Drude relaxation. Meanwhile, a sphere with the same resonance energy decays with  $T_2 \approx 1.4$  fs according to the measurement (see figure 14(b)). The faster dephasing rate is attributed to the  $\sim 80$  times greater volume of the sphere compared to the rod [120]. Under the assumption  $T_{nr,sphere} = T_{nr,rod}$  at the same resonance energy (here  $E_{res} = 1.7$  eV), we calculate the radiative rate of the sphere to be 1.5 fs. This short radiative lifetime would have significant implications in the discussion of optical antenna behaviour. According to this analysis, the rod shaped plasmonic antenna should be used to feed a load due to the lower overall dephasing rate,

and the sphere should be used to enhance radiative emission from a quantum source due to its high radiative decay rate. Other measurements reiterate this assumption of fast radiative decay [121]. Experimental efforts should be focused on direct radiative decay measurements to verify these assumptions.

It should be noted that the assignment of decay rates based on spectral amplitude measurements can be misleading as it relies on general assumptions of geometric and material homogeneity and lacks spectral phase information. Spectral line broadening can occur due to geometric variation within a measured inhomogeneous ensemble, local scattering points or roughness on individual particles, or absorption due to surface contamination, for example resulting in a shorter apparent relaxation time [55]. Additional information can be useful and should be collected when possible. For example, deviations in spectral phase behaviour from that expected for a harmonic oscillator could directly indicate the effects of intrinsic structural inhomogeneities on the underlying electron ensemble [122].

#### 6.4. Inconsistencies in plasmon radiative decay rate

Using a cavity model for resonances in gold plasmonic nanorods, the quantum efficiency  $\eta = \Gamma_r / (\Gamma_r + \Gamma_{nr})$  was calculated to vary over a wide range from about 0.05 to 0.8 depending on the effective plasmon wavelength which is related to the antenna geometry as shown in figure 15 for nanorods of radii  $R = 20, 10,$  and  $5$  nm for the cavity model (lines) and 3D numerical simulation (circles) [87]. The wavevector compression  $K = k'/k_0 = \lambda_0/\lambda_{\text{eff}}$  is related to the radius. The horizontal axis indicates the  $j$ th resonant mode for a given antenna length. In the quasistatic limit, appropriate for analysis of antennas with  $K \gg 1$ , the radiation resistance  $R_{\text{rad}}$  responsible for power lost through radiation is related to the radius  $R$  as  $R_{\text{rad}} \propto R^2$ . This trend agrees with the analysis discussed above for spheres where a greater  $\Gamma_r$  was associated with a greater particle volume. This suggests that if  $\Gamma_{nr}$  due to absorption does not increase significantly with radius, thicker antennas should have a greater quantum efficiency.

Nevertheless, there is some disagreement about the relative rates of the radiative and nonradiative decay channels in plasmonic nanorods. According to the analysis of [87], thicker rods exhibit greater  $\eta$  and lower wave surface binding (lower  $K$ ) as seen in figure 15. For an antenna with radius  $R = 20$  nm, the quantum efficiency is  $\eta = 0.8$ . This contradicts the measured scattering spectrum of [54], which shows that for a  $R = 20$  nm antenna with length  $L = 60$  nm (3:1 aspect ratio), the decay should be dominated by the nonradiative component, with the radiative efficiency being only 10% (see figure 14). Yet measurements of scattered radiation from arrays of  $L = 400$ – $525$  nm gold nanorods resulted in an estimated 82% radiative efficiency [123].

There are notable inconsistencies in theory as well. A semi-analytical model based on Pocklington's integral equation on a  $R = 5$  nm antenna indicates that 28% of the power delivered is lost via a radiative channel and 72% is absorbed [102], in good agreement with the finite element method solution of Maxwell's equations evaluated in the

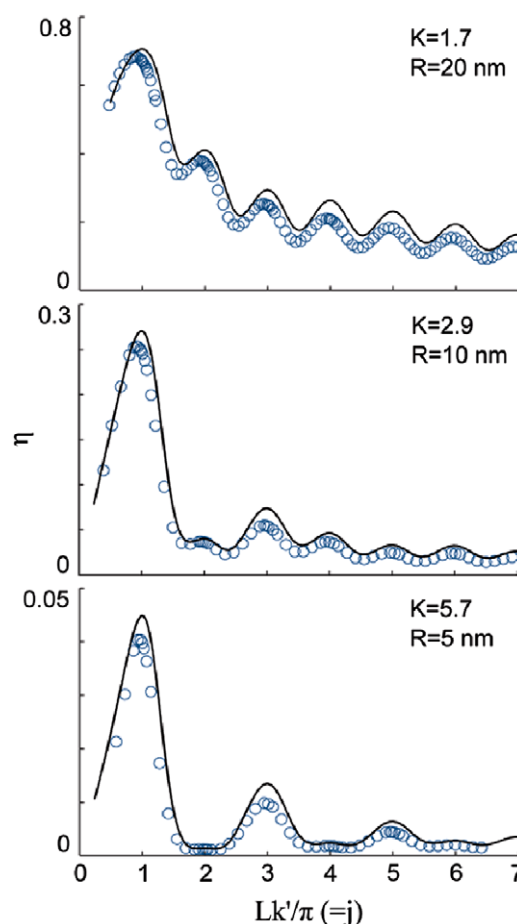


**Figure 15.** Calculated plasmonic nanorod quantum efficiency  $\eta = \Gamma_r / (\Gamma_r + \Gamma_{nr})$  as a function of length  $L$  ( $j$ th resonant mode) based on an analytical cavity model. Thicker rods (radius  $R$ ) exhibit greater  $\eta$  and lower surface wave binding (lower  $K$ ). Circles show results from numerical calculations. Reprinted with permission from [87]. Copyright 2011 American Chemical Society.

same work. On the other hand, a simple oscillator model can be applied to electrons in a plasmonic rod, accounting for radiation through the Abraham–Lorentz radiation reaction force. This model suggests that for a rod with average  $R = 90$  nm, the power associated with scattering or radiation is three times greater than the power associated with absorption near  $\lambda_0 = 7$   $\mu\text{m}$  [64]. This model agrees well with a finite-difference time domain (FDTD) simulation conducted in the same work.

The relative contributions of radiative versus nonradiative relaxation channels dominating plasmon decay thus seem to remain unclear. More investigation in this direction is needed also in order to better understand how antennas can enhance the radiative decay pathways of nanoloads. In particular, it is important to determine the relationship between antenna geometry, frequency of operation, and radiative relaxation rate.

#### 6.5. Relaxation dynamics in RF antennas

Relaxation rate presents a major inconsistency between RF and optical antenna behaviour. At frequencies far below the

Drude scattering rate ( $\omega \ll \gamma$ ), nonradiative decay channels due to Drude scattering become increasingly irrelevant in part due to the loosely bound nature of the RF surface wave, where a greater portion of the energy is outside the metal compared to the localized SPP case. The oscillation decay is therefore dominated by radiation. In contrast to the femtosecond timescale decay of optical antenna resonances, RF antennas exhibit decay times on the order of nanoseconds, as extracted from the linewidth of the radiative resistance [7, 10, 70, 124]. Since radiative resistance is wavelength dependent at these length scales (i.e., it is analysed in a wavelength-normalized reference frame) according to equation (5), the decay rate scales with the frequency of oscillation. Lower resonant frequencies thus correspond to lower radiative rates. For example, the quality factor,  $Q = f_{\max}/\Delta f$  (where  $f_{\max}$  is the resonant frequency), of a thin cylindrical antenna at its first open-circuit resonance is approximated from experimental data as  $Q \approx 3.5$  [70]. The resulting relaxation time of an  $L = 1$  m antenna is  $\tau = \tau_{\text{rad}} = 1/2\pi\Delta f = 1.8$  ns. This is comparable to the decay time found in time domain studies of linear antennas excited by short pulses [124]. The radiative relaxation time of RF antennas is several orders of magnitude greater than that of plasmonic antennas, highlighting the different energy scales and physical mechanisms at work in the different frequency regimes.

### 6.6. Enhancing atomic and molecular emission with antennas

Following the transformation associated field localization and enhancement, here we discuss various aspects related to the near-field coupling and energy transfer between an antenna and a quantum load in the RTC scheme. The spontaneous decay rate  $\Gamma_{\text{sp}}$  of, e.g., a quantum emitter such as an atom, molecule, or quantum dot, depends on the LDOS as described by equation (33). This is commonly known as Fermi's golden rule. The partial local density of states is given by [73]

$$\rho_{\mu}(\mathbf{r}_0, \omega_0) = \frac{6\omega_0}{\pi c^2} [\mathbf{n}_{\mu} \cdot \text{Im}\{\overleftrightarrow{\mathbf{G}}(\mathbf{r}_0, \mathbf{r}_0, \omega_0)\} \cdot \mathbf{n}_{\mu}] \quad (42)$$

where  $\mathbf{n}_{\mu}$  is the unit vector denoting the direction of the dipole moment  $\boldsymbol{\mu}_{21}$ . The Green's function  $\overleftrightarrow{\mathbf{G}}$  depends on the environment. It defines the relationship between a dipole moment  $\boldsymbol{\mu}$  at location  $\mathbf{r}'$  and its associated electric field at a different location  $\mathbf{r}$  as [61]

$$\mathbf{E}(\mathbf{r}) = \overleftrightarrow{\mathbf{G}}(\mathbf{r}, \mathbf{r}') \cdot \boldsymbol{\mu}(\mathbf{r}'). \quad (43)$$

Thus if the environment is changed (e.g., by a nearby antenna), the Green's function will change, and the decay rate of the quantum system can be modified. This can be achieved by placing the particle in a location with a high LDOS such as inside a Purcell cavity or near a plasmonic antenna in a region of high field enhancement.

The LDOS modification is not the only effect an antenna can have on the emission of a quantum system. In particular, coupling between a quantum emitter and an antenna can lead to four outcomes: (i) enhancement of the radiative rate of the emitter due to an increase in the LDOS through,

e.g., field enhancement near the antenna or constructive field interference; (ii) quenching of the radiative rate of the emitter due to a decrease in the LDOS through, e.g., destructive field interference; (iii) enhancement of the radiative rate due to the emitter coupling to fast radiative decay channels in the antenna; and (iv) quenching of the radiative rate due to the emitter coupling to fast nonradiant decay channels in the antenna [125].

Outcomes (i) and (ii) were observed experimentally via the change of radiative lifetime of the fluorescence decay of an emitter at various distances from a mirror [126, 127], or using the enhanced field near a gold nanoparticle to influence the radiative lifetime of a molecule [128] or quantum dot [45]. By scanning a gold nanoparticle in shear-force feedback over a  $10^{-9}$  molar concentration of terrylene molecules, a 22-fold increase in excited state decay rate was observed [57]. In another experiment, the radiative lifetime of an otherwise inefficient single molecule quantum emitter was shown to decrease by a factor of  $>28$  in the high energy density region between the elements of a coupled dimer bowtie nanoantenna, compared to the case without the antenna [60].

For molecular excitations with a low intrinsic radiative quantum yield, e.g., vibrational resonances in polyatomic molecules, direct mode transfer into an antenna system may result in competition between the intra- and intermolecular vibrational decoherence on one hand, and energy loss via the antenna's radiative channel on the other hand. If the antenna's radiative channel dominates, this is outcome (iii) [130]. Yet at small separation distances between the emitter and antenna, the radiative emission has been found to decrease significantly in some cases, particularly when the intrinsic quantum yield of the isolated particle is high. This quenching has been attributed to an increase in emitter coupling to dipolar and higher order modes in the antenna, providing new decay channels to the emitter. If the nonradiative channels dominate, quenching via outcome (iv) occurs [128, 129].

### 6.7. Quantum emitter impedance

In the context of the antenna-load coupling, the use of the LDOS as defined by the Green's function has been proposed as a way to describe antenna-load interactions in terms of impedance, linking traditional RF antenna terminology with that of quantum emitters [61]. This scheme is briefly summarized here. The time averaged power emitted by a radiating dipole  $\mathbf{p}(t) \propto \exp(-i\omega t)$  is

$$P_0 = \left\langle -\frac{d\mathbf{p}}{dt} \cdot \mathbf{E} \right\rangle = \frac{1}{2} \text{Re}(i\omega \mathbf{p} \cdot \mathbf{E}^*). \quad (44)$$

This equation is similar in form to the power dissipated by a load in a circuit,

$$P = \frac{1}{2} \text{Re}(IU^*), \quad (45)$$

where  $U$  is the voltage across the load and  $I$  is the current through it. Using the similarity between equations (44) and (45), a link between  $\mathbf{E}$  and  $U$ , and  $I$  and  $\mathbf{p}$  is established.

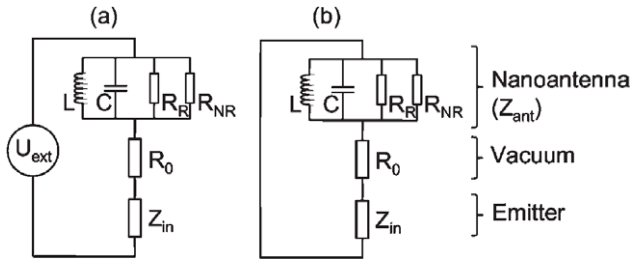


**Figure 16.** Coupling between a nanoantenna and an absorbing load (a) or emitter (b). Specific values for the circuit components depend on geometrical details and material parameters of their respective elements. Reprinted with permission from [61]. Copyright 2010 by the American Physical Society.

Then, inserting equation (43) into (44) the power emitted by the dipole is recast as

$$P_0 = \frac{1}{2} \text{Im} \frac{\vec{G}}{\omega} (\omega^2 |\mathbf{p}|^2). \quad (46)$$

An alternative form of equation (45) is

$$P = \frac{1}{2} \text{Re}(Z_L) |I|^2. \quad (47)$$

The similarity between these forms of  $P$  and  $P_0$  links  $\vec{G}$  to  $Z_L$ . The full set of transformations relates the optical  $\mathbf{p}$ ,  $\vec{G}$ , and  $\mathbf{E}$  to the electrical  $I$ ,  $Z$ , and  $U$  as

$$I \leftrightarrow -i\omega \mathbf{p}(\mathbf{r}) \quad (48)$$

$$Z \leftrightarrow -i \frac{\vec{G}(\mathbf{r}_0, \mathbf{r}_0, \omega)}{\omega} \quad (49)$$

$$U \leftrightarrow -\mathbf{E}_z(\mathbf{r}_0). \quad (50)$$

Note that in this formulation,  $I$  and  $U$  represent the current and voltage per unit length, and  $Z$  is impedance per unit area. Since  $\text{Re}(Z)$  represents  $\text{Im}(\vec{G})$ , the latter represents radiative and Ohmic losses in the quantum emitter–antenna. This can be understood since  $\text{Im}(\vec{G})$  is also proportional to the decay rate of the excited quantum emitter (see equations (33) and (42)). That is, a higher radiation resistance is related to a higher radiative decay rate.

The formulation above applies to the calculation of the radiated power emitted by a dipole into the field. The internal specific impedance of the quantum emitter itself is related to its polarizability as [61]

$$Z_{\text{in}} = \frac{i}{\omega \alpha \epsilon_0}. \quad (51)$$

Similarly, the specific impedance of a Purcell cavity [66] or an antenna can be determined from the known Green's function or polarizability, respectively.

Using these impedance transformations for the quantum system, the cavity, and the antenna, coupling between a cavity or antenna and a quantum emitter or absorber can be described in circuit diagram form. Figure 16 shows the equivalent circuit for an absorber (a) and emitter (b) coupled to a cavity or antenna. The emitter or absorber internal specific impedance is indicated as  $Z_{\text{in}}$ , the vacuum resistance is  $R_0$ , and the

nanoantenna or cavity impedance is the parallel combination of  $L$ ,  $C$ ,  $R_R$ , and  $R_{NR}$ , parameters dependent on geometric and material details of the antenna or cavity.  $U_{\text{ext}}$  represents the specific voltage introduced by an incident external field.

Notably, when the circuit corresponding to the antenna or cavity impedance is resonant, the impedance is purely real, and the ratio between the cavity or antenna resistance and the resistance of vacuum gives the Purcell factor, reflecting the increase or decrease in the density of states [61, 62]. There are general questions, however, on whether the Purcell factor can be applied accurately for plasmonic antennas. The absence of a defined set of normal modes for absorbing media, and nonresonant coupling of emission to higher order multipole moments not contained in a Purcell factor calculation, were reported to result in an underestimate of rate enhancement in plasmonic structures by up to an order of magnitude compared to a rigorous calculation based on the Green's function [62], and a deviation from the Purcell definition of effective mode volume has been calculated for larger particles [131]. The clarification of these and related questions could be the subject of future investigations.

## 7. Optical antennas as receivers

In section 6.7 we discussed the fundamental parameters relevant for antenna–nanoemitter coupling expressed in terms of impedance matching and emission rate enhancement. In that context, one of the core related functions of antenna systems is to receive EM radiation and provide the power at the position of the nanoload, which we shall discuss in this section.

Focusing optical energy below the diffraction limit has been achieved in several ways. Perhaps the simplest way is by exploiting the high electric field gradient associated with sharp geometric features on rough surfaces or on optically resonant nanostructures. Intensity enhancements of up to three orders of magnitude have been predicted in the gap between coupled linear dipolar resonators separated by a few tens of nanometres [132]. Alternatively, the electromagnetic interactions of proximate nanostructures have been controlled using femtosecond laser pulses shaped with respect to amplitude and temporal phase to produce high local field intensities in desired locations around the nanostructures [133, 134]. Nanofocusing has been proposed using similar plasmonic interactions driven instead by specially defined spatial phase profiles of superposed higher order Hermite–Gaussian modes [135] or plane waves [136].

In the following we examine yet another nanofocusing system based in particular on adiabatic nanofocusing on a conical tip as a model device to illustrate the general far-field to near-field RTC energy delivery system outlined in figure 2. We examine the system in terms of its performance and limitations and use it to discuss general metrics that may be used to benchmark antenna designs.

### 7.1. SPP focusing using optical antennas

SPP nanofocusing on a conical metal tip was originally proposed theoretically [25, 26, 137] and subsequently

implemented experimentally [30, 39, 42, 44, 49, 138, 139]. The topology of the regularly tapered 3D conical waveguide is unique in that it possesses only a single structural discontinuity at the very apex, minimizing opportunities for scattering losses. The gradual taper allows for a continuous adiabatic SPP mode transformation as the propagating SPP experiences an increasing effective index of refraction with decreasing cone radius. Associated with the increasing index of refraction is a decrease in group velocity and decrease in wavelength. This acts to compress the energy of the SPP spatially in the longitudinal direction. Low-loss SPP compression relies on a smooth geometrical transformation satisfying the adiabatic condition  $\partial \ll 1$  where  $\partial = |d(k_{\text{SPP}})^{-1}/dr| \tan(\theta)$  is the adiabatic parameter describing the rate of change of the SPP wavevector with wire radius  $r$  and tip half cone angle  $\theta$  [30]. The narrowing cone also acts as a mode filter, as only the radially symmetric  $m = 0$  mode can propagate all the way to the apex.

This technique has been implemented using electrochemically etched conical gold tips as shown in figure 17(a) [39, 42, 49, 138, 139]. To excite SPPs, a grating was cut into the surface of the tip shaft as a coupling element using focused ion beam (FIB) milling [81]. At the tip apex, the adiabatic condition ultimately breaks down and the energy from the SPPs is radiated in the form of a dipolar nanoemitter oriented parallel to the tip axis [42]. The spot size of this emitter was measured as  $\sim 20$  nm (FWHM) using s-SNOM.

Antenna-to-load coupling of the nanofocused point dipole of the tip to a molecular dipole load [49] and silicon nanocrystal [138] was demonstrated in tip-enhanced Raman spectroscopy. The small emitter size and nonlocal grating excitation mechanism were shown to allow for nanometre spatially selective excitation and to substantially suppress unwanted background signal.

In field localization techniques that utilize the sculpted temporal phase of short pulses to drive coherent oscillations on plasmonic structures, the waveforms of the pulses are constrained by the interference requirements, allowing for spatial confinement, but not arbitrary temporal pulse shaping [133, 134]. Simultaneous control of the spatial and temporal profile of picosecond pulses has been achieved by shaping the spatial phase of the light propagating through a complex medium [140]. However, in both of these methods the temporal or spatial shaping is sample dependent. The conical nanoantenna concept separates spatial and temporal control of the optical field, allowing for arbitrary temporal waveform generation at the apex nanoemitter, decoupled from the sample geometry and spatial or temporal phase constraints inherent in other specific field localization techniques. The pulse spectral phase is defined prior to grating illumination using a pulse shaper and optimized via a multiphoton intrapulse interference phase scan (MIIPS) algorithm, as shown in figure 17(b) [44]. The corresponding tip emissions at the fundamental and second harmonic frequencies are shown in figure 17(c) and the reconstructed optical waveform of the tip emission with 16 fs duration as an example for a short pulse is shown in figure 17(d). The ability to generate arbitrary waveforms is limited only by the spectral bandwidth that can be coupled by the spatially chirped grating coupling element.

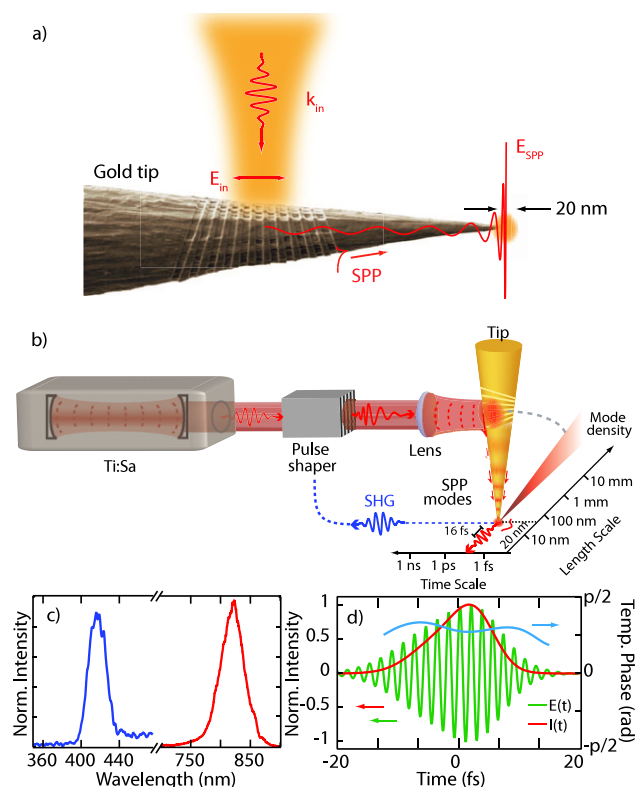


**Figure 17.** SPP nanofocusing. (a) A conical metal tip optical antenna. The SPP nanofocusing tip demonstrates the three elements of an optical antenna: collection, confinement, and delivery to a load. Incident light is collected by a grating SPP coupler. The SPP propagates towards the apex, experiencing adiabatic energy compression with decreased waveguide radius. The SPP finally emits radiation from a 20 nm sized spot at the cone apex. (b) Nanofocusing of ultrafast pulses using the conical geometry. The pulses emitted at the apex are defined by a pulse shaper with feedback on the tip second harmonic generation emission allowing for arbitrary ultrafast waveform control from a nanoscale emitter. (c) Spectrum showing the fundamental and second harmonic light emitted at the apex. (d) Reconstructed optical waveform of the nanofocused ultrashort laser pulse with 16 fs duration. Adapted with permission from [30]. Copyright 2012 American Chemical Society.

*Nonadiabatic* propagating SPP nanofocusing has been demonstrated on wedges [141] and coplanar structures [142] as shown in figure 18. These structures are useful in planar geometries for feeding plasmonic waveguides or in situations where a load can be precisely placed at the focus as with metal–oxide–metal diodes [114]. However, they are susceptible to significant scattering losses at edges and corners and it has yet to be shown to what extent they can outperform simpler geometries such as linear-coupled rods or bowties.

As an optical antenna, the conical SPP nanofocusing structure has several advantages. Although the coupling grating must be designed for a specific coupling wavelength and bandwidth, the adiabatic mechanism is intrinsically broadband. The structure permits the transmission and spatial compression of ultrashort pulses, allowing the implementation of this antenna design for time-resolved applications [44]. Also, the conical design is readily implemented as a scanning probe ideal for, e.g., tip-enhanced Raman spectroscopy [49].

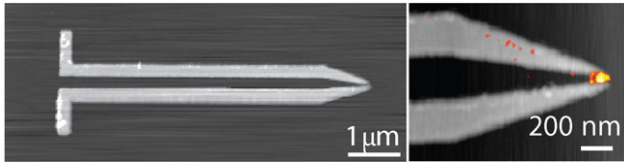


**Figure 18.** Plasmonic nonadiabatic nanofocusing using an antenna-coupled coplanar stripline in the mid-IR. Light incident on the linear antenna (left) excites a travelling wave on the stripline. A taper at the end of the line concentrates the light, creating a nanofocused spot. Adapted with permission from [142]. Copyright 2011 by Macmillan Publishers Ltd: Nature Photonics.

However, this structure has limitations too. For one, the waveguide propagation introduces loss. Moreover, while the grating is a suitable receiver for far-field excitation and capture, the grating coupler capture cross section is equivalent to its physical cross section in contrast to, e.g., linear antennas [6].

### 7.2. Antenna performance metrics

The example of the conical antenna highlights the need for a way to systematically compare different antenna designs. In particular, specific, broadly applicable performance metrics would facilitate optimized engineering strategies.

Figure 19(a) shows several nanofocusing optical antenna architectures including a spherical plasmonic particle, a quantum system, a plasmonic bowtie, and a conical SPP waveguide. Despite the different form factors, these all have the same underlying functionality in receiving mode as shown in figure 19(b). The three step RTC transformation process is characterized by several parameters. Incident light of intensity  $I_{\text{in}}$  is captured by a receiving element with receiving cross section  $\sigma_r$ , which may be several times bigger than the physical area  $A_r$  of the receiver. Each RTC step is characterized by a power  $P_r$ ,  $P_t$ , and  $P_c$ , respectively, and an efficiency  $\eta_r = P_r/P_{\text{in}} = \sigma_r/A_r$ ,  $\eta_t = P_t/P_r$ , and  $\eta_c = P_c/P_r$ . Ohmic and radiative losses are accounted for by  $R_r$ ,  $R_t$ , and  $R_c$ , respectively. Breaking up the nanoscale energy delivery function of the optical antenna into three parts allows for the characterization and optimization of each section individually.

Even so, a single performance metric describing the entire conversion process from reception to load coupling can be assigned as the total energy delivery efficiency given by

$$\eta_{\text{tot}} = \eta_c \eta_t \frac{\sigma_r}{A_r}. \quad (52)$$

Previously, the field enhancement of the optical antenna has been used as a primary metric. The field enhancement can be described in our current terminology as

$$F = \frac{|E_t|}{|E_0|} = \sqrt{\frac{I_t}{I_{\text{in}}}} = \sqrt{\frac{P_t/A_t}{P_{\text{in}}/A_r}} \quad (53)$$

where  $E_t$  is the electric field at the end of the transformation section,  $E_0$  is the free-space electric field, and  $I_t = c\epsilon_0 n |E_t|^2 / 2$  is the intensity at the end of the transformation.  $A_t$  is the size

of the enhanced field region, defined as  $A_t = 4d_1d_2$ , where  $d_1$  and  $d_2$  are the half-widths at half-maximum of the intensity of the enhanced field in the  $x$ - and  $y$ -directions, respectively, as shown in figure 19(c). Field enhancement has been the most commonly employed metric, yet it is incomplete. It is sufficient when the source power is not the limiting factor, which may be the case in some spectroscopy applications, but is not the case in general and for most cases where optical antenna designs are most needed to, e.g., enhance small signals, or redefine emitter directivity. The total efficiency  $\eta_{\text{tot}}$  may be advantageous over  $F$  as an overall performance metric, because it takes into account the physical and effective size of the antenna, as well as coupling efficiency to the load.

Some of the parameters embedded within these performance metrics are easily accessible, such as the receiver physical area  $A_r$  and incident intensity  $I_{\text{in}}$ . Others such as the power after transformation  $P_t$  and the area of the focused light  $A_t$  could be measured using special instrumentation such as near-field microscopy [42, 142]. Field enhancement  $F$  can be rewritten to shed light on the efficiencies as  $F^2 = \eta_r \eta_t A_r / A_t$ .  $\eta_c$  may be determined from, e.g., knowledge of the radiative and nonradiative decay channels of the load and careful measurement of its radiated power. We acknowledge that some of these parameters may be difficult to access, but the search for suitable measurement techniques is a desirable research goal in itself.

## 8. Measuring antenna parameters at optical frequencies

All three steps of the RTC process are associated with evanescent fields that can shed light onto the respective underlying RTC parameters. In this section we consider the state of the art of antenna far-field and near-field measurement methods. In particular, we focus on the near-field vector network analyser (VNA), a tool capable of providing full electromagnetic near-field information about an antenna with nanometre scale spatial resolution.

Far-field measurements can provide information about the interaction between an antenna and propagating light. As one example, the relationship between device geometry and resonant frequency can be measured using visible and IR transmission or extinction spectroscopy [92–94, 143, 144]. Second, as in the RF, the emission direction of optical antennas can be controlled, promising enhanced detection of, e.g., quantum emission [145]. The directivity of antenna-coupled molecular emission [47] and Yagi–Uda antennas operating at optical frequencies [146] has been measured using high numerical aperture optical microscopy. Third, field enhanced regions near plasmonic particles where nanoloads can be located can be identified by imaging the enhanced region's point spread function using two-photon photoluminescence [96, 147, 148] or nonlinear response [121, 122], though the imaging resolution can still be limited by diffraction to a few hundred nanometres. In the infrared, antenna-coupled bolometers have been used to measure the polarization response [149] or capture efficiency of antennas as a function of frequency and angle of incidence of an excitation beam [34, 35].

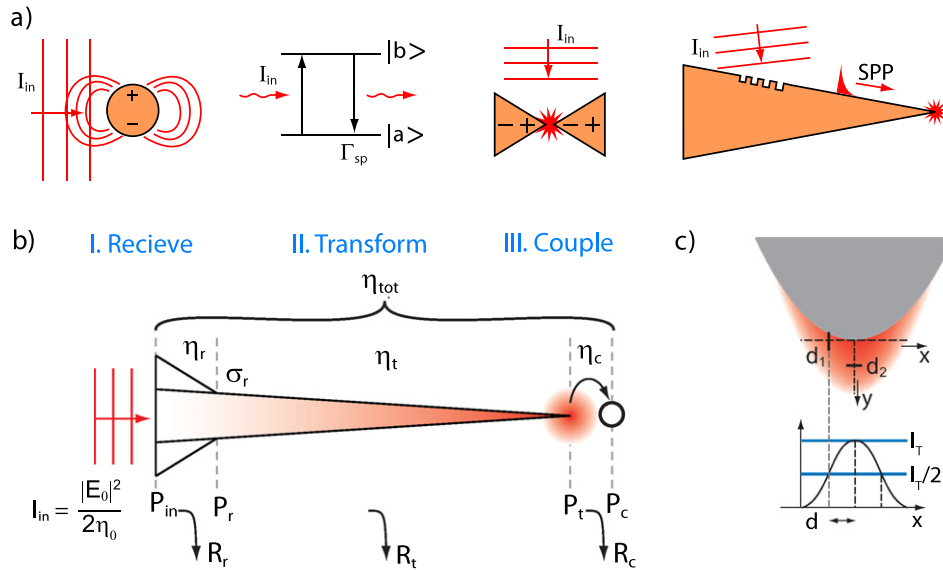


**Figure 19.** Comparing performance of optical antennas. (a) Optical antennas in different forms including a plasmonic dipole, a two-level quantum system, a plasmonic bowtie, and a surface plasmon nanofocusing element. (b) A generalized schematic diagram of the three-component receiving antenna including reception, transformation, and coupling to a nanoload. Important parameters of this process include the receiver cross section  $\sigma_r = P_r/I_{in}$ , the receiving, transforming, and coupling efficiencies  $\eta_r$ ,  $\eta_t$ , and  $\eta_c$ , respectively, and the power at the end of each stage  $P_r$ ,  $P_t$ , and  $P_c$ . Power losses at each stage are indicated as  $R_r$ ,  $R_t$ , and  $R_c$ . (c) Nanofocus area  $A_t$  is evaluated using the half-power distances  $d_1$  and  $d_2$  associated with the decay in  $\hat{x}$  and  $\hat{y}$ , respectively, as  $A_t = 4d_1d_2$ .

Electronic techniques can facilitate the extraction of spatially detailed information required to optimize nanoparticle geometry for a targeted near-field profile. For example, electron energy loss spectroscopy (EELS) implemented in a scanning transmission electron microscope has been used to characterize plasmonic field enhancement with nanometre resolution [106]. Photocurrent measurements have been used to identify and quantify locally enhanced fields [150]. Cathodoluminescence has been used to create monochromatic emission maps of silver nanoprisms, resolving the plasmon mode on a length scale of 25 nm [151]. Photoemission electron microscopy (PEEM) delivers high spatial and temporal resolution, allowing for, e.g., the measurement of the temporally resolved plasmonic response of a multi-element metallic nanostructure [134, 152]. Optical near-field techniques can offer complementary information about the local electric field magnitude and phase with nanometre spatial resolution allowing one to correlate details of the field with nanometre scale geometrical features. These techniques can be used to image plasmonic resonances. A short review of plasmonic resonance imaging methods can be found in [152].

In order to achieve optical resolution below the diffraction limit, one must interrogate the sample of interest in its near-field before evanescent field components associated with high spatial frequency decay significantly. Scanning near-field optical microscopy (SNOM) is a scanning probe technique used to measure optical fields with resolution below the diffraction limit. It can be divided into two main schemes. The first uses light transmission through an aperture often at the tip of a pulled optical fibre [153–155]. The other, so-called apertureless or scattering-type SNOM (with the corresponding equivalent appellations a-SNOM or s-SNOM),

utilizes the sharp apex of a scanning probe tip (e.g. an atomic force microscope tip) to interrogate the near-field, scattering the light to a detector [156–159]. In both modes of operation, the probe is held in close proximity to the sample by force feedback. The tip-sample region is illuminated by an external light source either through the tip (in the case of SNOM), through the sample, or through free space, typically focused by a lens or mirror. Nanometre spatial imaging resolution is achieved by collecting or scattering signal light from only the region near the probe tip. In aperture based SNOM this presents a trade-off between optical throughput and imaging resolution, which are both largely defined by the aperture size. The resolution of s-SNOM, on the other hand, is limited only by the tip dimensions, with typical curvature at the apex of  $\sim 10$  nm in radius [158–160]. Moreover, lifting the requirement for transmission through optical fibres, s-SNOM can be implemented with light frequencies from microwave through optical [161, 162].

SNOM in both its operating modes has been very useful for learning about the resonant modes of plasmonic antennas. It has been used to measure antenna modes in the visible [12] and infrared [97–99], including higher order plasmonic resonances [85], coupling between antennas and nanowire waveguides [113], nanofocusing and field enhancement [142], dark and bright modes of plasmonic metamolecules [163] and amplitude and phase of the different elements of an optical Yagi–Uda antenna [164], for example.

## 9. The near-field vector network analyser

While all of the techniques discussed above provide valuable information about optical antennas, full electromagnetic

characterization capabilities comparable to those available for RF antennas are still being developed. New tools are required for routine characterization of antenna parameters such as input impedance, current distribution, local magnetic field, and local electric field.

In conventional measurement of RF device electromagnetic parameters, the magnitude and phase of the potential at the input of a scanning probe antenna, typically a small dipole or loop, is measured using a vector network analyser (VNA) or a spectrum analyser with a known reference frequency. The probe acts as the receiver with the VNA measuring in transmission mode [165]. The probe is scanned in the volume around the antenna under test (see figure 21(a)). The received signal is related to the electric or magnetic field amplitude and phase at the location of the probe. The polarization of the fields can be measured by the selective orientation of the probe dipole. These types of scanning microwave probe system have been implemented to measure conductivity of stratified media and to probe subsurface features [166].

Extending this technique to optical frequencies would be very helpful for optical antenna engineering. Notably, one need not gain direct access to each individual EM parameter in order to gain a full understanding of the electronic nature of a plasmonic antenna. This is important because, while the electric field is readily accessible, as will be demonstrated below, the optical magnetic field is somewhat more difficult to access experimentally due to the weaker Lorentz force associated with the magnetic light–matter interaction, compared to the Coulomb interaction. The electric vector field  $\mathbf{E}$  and magnetic field  $\mathbf{H}$  of the time-varying optical electromagnetic wave are related by the Maxwell–Faraday equation.

$$\mathbf{H}(\mathbf{r}) = -\frac{i}{\omega\mu_0} \frac{\partial \mathbf{B}(\mathbf{r})}{\partial t} = \frac{i}{\omega\mu_0} \nabla \times \mathbf{E}(\mathbf{r}). \quad (54)$$

Here we use the constitutive relation  $\mathbf{B} = \mu_0 \mathbf{H}$  and the fact that the time derivative of a time-harmonic wave can be represented instead as a multiplication by  $i\omega$  where  $\omega$  is the frequency of the wave. Similarly, the Maxwell–Ampère equation links  $\mathbf{E}$  and  $\mathbf{H}$  to the current density  $\mathbf{J}$  as

$$\nabla \times \mathbf{B}(\mathbf{r}) = \mu_0 \left( \mathbf{J} + \epsilon_0 \frac{\partial \mathbf{E}(\mathbf{r})}{\partial t} \right). \quad (55)$$

Thus if one knows the precise electric field in great detail, the other electromagnetic parameters may also be determined.

### 9.1. Dipole current density recovery

Full knowledge of the electric field distribution allows for the determination of current density as described here for a linear dipole antenna. Any source current  $\mathbf{J}(\mathbf{r})$  for electromagnetic fields can be considered as composed of a superposition of point currents with the resulting  $\mathbf{E}(\mathbf{r})$  and  $\mathbf{H}(\mathbf{r})$  fields generated by integrating over all the sources in a volume  $V$  [73],

$$\mathbf{E}(\mathbf{r}) = \mathbf{E}_0(\mathbf{r}) + i\omega\mu_0 \int_V \overleftrightarrow{\mathbf{G}}(\mathbf{r}, \mathbf{r}') \mathbf{j}(\mathbf{r}') dV' \quad (56)$$

$$\mathbf{H}(\mathbf{r}) = \mathbf{H}_0(\mathbf{r}) + \int_V \left[ \nabla \times \overleftrightarrow{\mathbf{G}}(\mathbf{r}, \mathbf{r}') \right] \mathbf{j}(\mathbf{r}') dV' \quad (57)$$

with the homogeneous solutions of the wave equation  $\mathbf{E}_0(\mathbf{r})$  and  $\mathbf{H}_0(\mathbf{r})$ . Thus the current represents the fundamental source of the resulting EM fields. The dyadic Green’s function relates the field at position  $\mathbf{r}$  to the source current at position  $\mathbf{r}'$  and it is given by

$$\overleftrightarrow{\mathbf{G}}(\mathbf{r}, \mathbf{r}') = \left[ \overleftrightarrow{\mathbf{I}} + \frac{1}{k^2} \nabla \nabla \right] \frac{e^{\pm ik|\mathbf{r}-\mathbf{r}'|}}{4\pi|\mathbf{r}-\mathbf{r}'|} \quad (58)$$

where  $\overleftrightarrow{\mathbf{I}}$  is the unit dyad. Although the constitution of fields from current source elements is straightforward, the reverse problem, namely determining the current source elements from the fields, is more complicated. It has been worked out previously, however [9], as discussed next.

*9.1.1. Hallén’s integral equation.* To solve for the current density distribution on a linear conductor, given the electric near-field, one may turn to the vector potential as an intermediate parameter. The advantage of using the vector potential instead of the electric field to solve for the current density distribution is that each component of the current density distribution results in a vector potential component in the same coordinate. That is, an  $\hat{x}$ -oriented source current  $J_x = \mathbf{J} \cdot \hat{x}$  results in an  $\hat{x}$ -oriented vector potential, but results in an electric or magnetic field with  $\hat{x}$ ,  $\hat{y}$ , and  $\hat{z}$  components in general [70]. The vector potential  $\mathbf{A}(\mathbf{r})$  is defined with

$$\mathbf{B}(\mathbf{r}) = \nabla \times \mathbf{A}(\mathbf{r}), \quad (59)$$

and the Lorenz gauge,

$$\nabla \cdot \mathbf{A}(\mathbf{r}) = i\omega\mu\epsilon\phi(\mathbf{r}). \quad (60)$$

The quantity  $\phi(\mathbf{r})$  is the scalar potential, providing an alternative form of the EM fields in an infinite medium,

$$\mathbf{E}(\mathbf{r}) = i\omega\mathbf{A}(\mathbf{r}) - \nabla\phi(\mathbf{r}), \quad (61)$$

$$\mathbf{H}(\mathbf{r}) = \frac{1}{\mu_0\mu_r} \nabla \times \mathbf{A}(\mathbf{r}). \quad (62)$$

With the potential functions fully defined, the vector potential is related to the current through the Helmholtz equation,

$$[\nabla^2 + k^2]\mathbf{A}(\mathbf{r}) = -\mu\mathbf{J}(\mathbf{r}) \quad (63)$$

The distribution of axial current is independent of the shape of the antenna cross section if the maximum dimension is small compared with the wavelength [70]. As an example, the width of the  $f_0 \approx 30$  THz antenna studied in [167] is about  $\lambda/70$ . Approximating the current density  $\mathbf{J}(\mathbf{r})$  as a line current flowing in the  $\hat{y}$  direction, the local current  $I(y')$  is related to the vector potential at the surface of the antenna. The solution to the Helmholtz equation is

$$A_y(y) = \frac{\mu}{4\pi} \int_{-L/2}^{L/2} I(y') G(y-y') dy'. \quad (64)$$

Then, with the relation between  $A_y$  and  $E_y$ ,

$$\left( \frac{\partial^2}{\partial y^2} + k^2 \right) A_y(y) = -i\omega\mu\epsilon E_y(y), \quad (65)$$

the solution for the current is determined directly from the measured electric near-field antenna-parallel component  $E_y$  by solving Hallén's integral equation,

$$\frac{\mu_0}{4\pi} \int_{-L/2}^{L/2} I(y') G(y - y') dy' = i\omega\mu\epsilon(\partial_y^2 + k^2)^{-1} E_y(y) \quad (66)$$

where  $L$  is the antenna length in wavelengths,  $k^2 = \omega^2/\mu\epsilon$ , and  $G(y - y') = e^{ikR}/(4\pi R)$ , is the reduced thin wire kernel with  $R = \sqrt{(y - y')^2}$  [6, 9, 70]. This equation can be solved numerically by the method of moments [9].

In a general formulation of the method of moments, the desired quantity  $g$  is broken up into  $N$  segments along the solution geometry, each with a coefficient  $a_n$ . The equation of interest (e.g. the integral equation here) is reformulated with the discrete elements as [6]

$$\sum_{n=1}^N a_n F(g_n) = h_m \quad (67)$$

where  $F$  is a linear operator and  $h$  is the known quantity with  $m = 1, 2, 3, \dots, N$  elements. Each  $g_n$  takes the form of a basis function (pulse, triangle, sinusoid, etc) with unknown amplitude  $a_n$ . The basis function is chosen, and the system of linear equations is solved for the quantities  $a_n$ .

## 9.2. Vector field measurements

Using Maxwell's equations, the time-dependent THz electric field, magnetic field, and Poynting vectors of a slit array were determined in the near-field using Fourier transform imaging [168]. In this method, the time domain transients corresponding to two orthogonal ( $E_x$  and  $E_z$ ) electric field vector components in the plane perpendicular to the sample surface were measured by electro-optic sampling. The spectral amplitude and phase at each pixel above an array of slits was determined by Fourier transform analysis of the temporal transients. In this way, the electric field was fully characterized, allowing for calculation of the magnetic field and Poynting vectors. Figure 20 shows the electric field in the  $x$ - $z$  plane and the corresponding magnetic field at 1 THz using this technique. A similar approach was demonstrated at  $\lambda = 660$  nm to measure the vector distributions of Bessel beams, but the electric field components were measured in a plane parallel to a sample surface, not perpendicular to it [169]. The temporal evolution of the vector components in the volume away from the sample plane could be extrapolated numerically to determine the complete 3D field distribution.

Full electromagnetic characterization capabilities can be extended to the optical regime by taking inspiration from RF design tools. Figure 21(a) shows a schematic diagram of the VNA being used to measure the near-fields of an antenna under test using a small probe antenna as discussed above. The key of this technique is the ability to measure the fields with amplitude, phase, and vector orientation. s-SNOM, mentioned above as a technique for imaging resonant modes of plasmonic particles, is also capable of measuring amplitude, phase, and vector orientation. As shown in figure 21(b), a portion of excitation light is redirected for

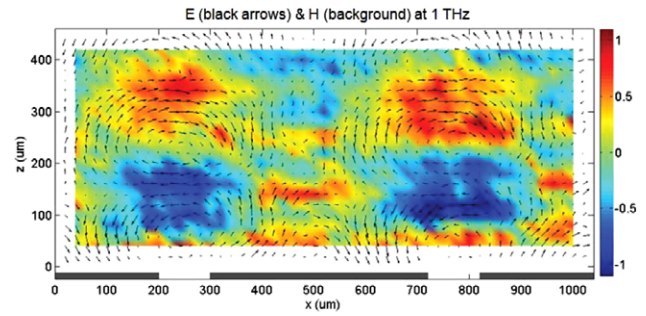


**Figure 20.** Measured full vectorial representation of transmission through a slit. Two orthogonal electric field components in the  $x$ - $z$  plane fully define the electromagnetic character of the transmitted light. The magnetic field vectors are then deduced using Maxwell's equations. Reprinted with permission from [168]. Copyright 2007 Optical Society of America.

use as a phase reference. Near-field light is scattered by the probe tip to the detector. The interference signal between the tip-scattered light and the reference contains phase and amplitude information. It can thus be considered the optical analogue of the RF VNA, or the nano-optical VNA [167].

In early vector imaging efforts, a gold nanoparticle on a fibre probe tip was used to scatter near-field light to a detector. The near-field vector angle, but not direction, of elliptically polarized light could be deduced [170]. Later, s-SNOM was used to measure the electric vector distribution of the field of aperture bowtie antennas, demonstrating the capability of measuring the full phase-resolved electric field [171].

Despite the weaker magnetic force, efforts have also been made to directly measure the optical magnetic field  $\mathbf{H}(\mathbf{r})$  with scanning probe tips. The magnetic field intensity was measured in the optical near-field via excitation of a ring plasmon in gold coated probe tips [172]. A measurement of  $\mathbf{H}(\mathbf{r})$  has also been reported using a split-ring resonator at the end of a scanning probe tip [173]. These types of tip have yet to be implemented for scanning optical antennas, as both their fabrication and the resulting signal interpretation, can be challenging.

The nano-optical VNA was used to determine the electric field, magnetic field, and current density distributions of a linear-coupled dipole antenna [167]. Figure 21 shows a scanning electron microscope image of a linear coupled-dipole antenna (c) and its electric vector near-field measured by s-SNOM (d) with amplitude and vector orientation indicated by the arrows and signal magnitude  $|S| = (S_y^2 + S_z^2)^{1/2}$  indicated by the colorbar. An inset shows the rotation of the vector field at the large field gradient near the antenna gap of  $\approx 80$  nm associated with a high field enhancement factor of about 30. Access to arbitrary vector components was achieved by nano-engineering the probe tip for increased scattering sensitivity to tip-perpendicular field components. Equation (54) allowed the determination of the corresponding magnetic field and Hallén's integral equation was used to obtain  $\mathbf{J}$  directly from  $\mathbf{E}$  as shown in figures 21(e) and (f) for experiment and theory, respectively.

The result for the current shows a two-sided, nearly symmetric distribution centred on each dipole as expected

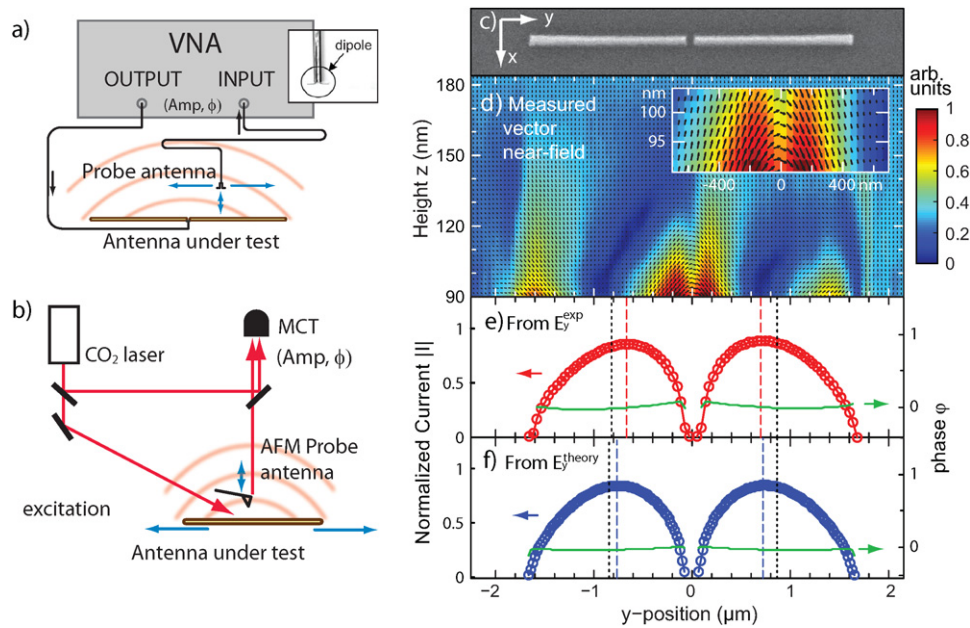


**Figure 21.** Vector near-field imaging of optical antennas for determination of electromagnetic parameters. (a) A schematic diagram of the RF vector network analyser capable of measuring antenna near-fields with amplitude and phase information (dipole probe inset used with permission from [165], copyright 2007 IEEE). (b) The parallel implementation of (a) at optical frequencies using s-SNOM. (c) SEM image of a gold linear coupled-dipole optical antenna resonant at  $\lambda_0 = 10.6 \mu\text{m}$ . (d) Vector near-field as measured by a phase sensitive s-SNOM based nano-optical vector network analyser. Colour indicates field magnitude. Inset: Close-up view of field orientation near the gap at  $y = 0 \mu\text{m}$ . (e) Normalized current magnitude determined solving Hallén's integral equation using experimental near-field data. (f) Current calculated from theory. The current distribution exhibits a peak shift (red or blue dashed lines) from the geometrical centre of the rod (black dashed lines) towards the gap, indicating coupling between the rods.

to first order for this geometry. The peak shift seen in the current distribution in figure 21(e) and the corresponding theory 21(f) results from interdipole antenna coupling associated with Coulomb interactions across the gap.

This example demonstrates that if  $\mathbf{E}$  is known in sufficient detail, one may calculate the associated  $\mathbf{H}$  and  $\mathbf{J} \propto \mathbf{I}$ . Though simplified here for the case of a linear antenna geometry, these operations are general and can readily be extended for the determination of magnetic field and current from 3D near-field data for arbitrary antenna geometries. This demonstrates the implementation of phase-resolved s-SNOM as a VNA for nano-optical applications, bringing this important RF design tool to the optical regime.

In an extension of this instrument's capabilities, heat dissipation can also be characterized. Loss of energy to heat can be detrimental to optical antenna functionality, as each RTC building block suffers from it with its own different loss mechanism. s-SNOM using vector imaging techniques can be used to measure the thermal near-field of an antenna, and thereby acquire local information about the heat dissipation throughout the structure [174].

## 10. Conclusion and outlook

In summary, we have reviewed the physical basis of the light-matter interaction at the transition from the RF to optical regime, discussing the extension of antenna theory from the RF to optical as is required for the development of optical antenna design strategies. We gave an overview of RF antenna

theory including resonance and impedance and discussed the range and limitations in its applicability for optical antenna design. We have discussed impedance at optical frequencies as it is understood for optical gap antennas as well as a local density of states formulation that has been suggested for loads or sources in arbitrary locations in the antenna near-field.

We have generalized the ideal antenna-load interaction through a transformation process composed of three main steps: (i) reception of far-field light and subsequent excitation of an extrinsic antenna resonance, (ii) transformation and localization of the captured energy, and (iii) near-field coupling to a quantum load, comprising the RTC scheme.

This general scheme was illustrated as an example by application to a conical SPP focusing optical antenna. Motivated by the need for a tool for systematic comparison between different optical antenna architectures, we have proposed a performance metric for maximizing conversion efficiency from far-field light to a nanolocalized excitation at a load. The overall efficiency can be decomposed into parameters describing the power and efficiency of each building block of the RTC system, allowing for individual characterization and optimization of each subfunction of the antenna. While new measurement methods will help measure the performance of optical antennas, many of the metric parameters can already be accessed using, e.g., a near-field vector network analyser. Towards this end, we discussed the full near-field EM characterization of an infrared optical antenna.

We hope this review will give a perspective to the discussion of antenna-load interactions at optical frequencies

in terms of ideas that can be carried over from RF antenna engineering as well as new design strategies related to the quantum nature of nanoantennas and nanoloads. We have identified several areas where further investigation would benefit optical antenna design. Specifically, the radiative and nonradiative decay channels associated with quantum emitter–antenna coupling should be examined to determine how they relate to different geometries and materials. The density of states formalism and validity of the Purcell factor analogy for optical antennas should be verified experimentally for spheres as well as more sophisticated geometries. LDOS impedance concepts should be formulated for new optical antenna geometries beyond the sphere such as the conical waveguide, linear dipole, and patch antenna. Finally, experimental techniques for antenna characterization should be developed for routine analysis.

## Acknowledgments

The authors gratefully acknowledge inspiring discussions with Samuel Berweger and Carsten Rockstuhl, and fruitful interactions with Brian Lail and Glenn Boreman and his team. Funding from the National Science Foundation (NSF CAREER grant CHE0748226, grant ECCS-1204993, and NSF IGERT Program) and the Innovative Seed Grant Program at the University of Colorado is gratefully acknowledged.

## References

- [1] Dressel M and Grüner G 2002 *Electrodynamics of Solids* (Cambridge: Cambridge University Press)
- [2] Ashcroft N W and Mermin N D 1976 *Solid State Physics* (Orlando, FL: Harcourt)
- [3] van de Hulst H C 1981 *Light Scattering by Small Particles* (New York: Dover)
- [4] Maier S A 2007 *Plasmonics: Fundamentals and Applications* (Berlin: Springer)
- [5] Bohren C F and Huffman D R 1983 *Absorption and Scattering of Light by Small Particles* (Mörlenbach: Wiley-VCH)
- [6] Balanis C A 1997 *Antenna Theory: Analysis and Design* 2nd edn (New York: Wiley)
- [7] Stutzman W L and Thiele G A 1997 *Antenna Theory and Design* 2nd edn (New York: Wiley)
- [8] Pozar D 2005 *Microwave Engineering* 3rd edn (Hoboken, NJ: Wiley)
- [9] Orfanidis S J 2011 Electromagnetic waves and antennas [www.ece.rutgers.edu/~orfanidi/ewa/](http://www.ece.rutgers.edu/~orfanidi/ewa/)
- [10] Schelkunoff S A and Friis H T 1952 *Antennas: Theory and Practice* (New York: Wiley)
- [11] IEEE Standards Board 1993 IEEE standard definitions of terms for antennas (IEEE Std 145-1993) *Tech. Rep.*
- [12] Rang M, Jones A C, Zhou F, Li Z Y, Wiley B J, Xia Y and Raschke M B 2008 *Nano Lett.* **8** 3357–63
- [13] Fumeaux C and Herrmann W 1998 *Infrared Phys. Technol.* **39** 123–83
- [14] Alda J, Rico-García J M, López-Alonso J M and Boreman G 2005 *Nanotechnology* **16** S230–4
- [15] Park Q H 2009 *Contemp. Phys.* **50** 407–23
- [16] Bharadwaj P, Deutsch B and Novotny L 2009 *Adv. Opt. Photon.* **1** 438
- [17] Giannini V, Fernandez-Dominguez A I, Heck S C and Maier S A 2011 *Chem. Rev.* **111** 3888–912
- [18] Biagioni P, Huang J S and Hecht B 2012 *Rep. Prog. Phys.* **75** 024402
- [19] Novotny L and van Hulst N 2011 *Nature Photon.* **5** 83–90
- [20] Berkovitch N, Ginzburg P and Orenstein M 2012 *J. Phys.: Condens. Matter* **24** 073202
- [21] Agio M 2012 *Nanoscale* **4** 692–706
- [22] Liu Z, Steele J M, Srituravanich W, Pikus Y, Sun C and Zhang X 2005 *Nano Lett.* **5** 1726–9
- [23] Lindquist N C, Nagpal P, Lesuffleur A, Norris D J and Oh S H 2010 *Nano Lett.* **10** 1369–73
- [24] Volpe G, Volpe G and Quidant R 2011 *Opt. Express* **19** 3612–8
- [25] Babadjanyan A J, Margaryan N L and Nerkararyan K V 2000 *J. Appl. Phys.* **87** 3785
- [26] Stockman M 2004 *Phys. Rev. Lett.* **93** 137404
- [27] Verhagen E, Kuipers L and Polman A 2007 *Nano Lett.* **7** 334–7
- [28] Vogel M and Gramotnev D 2007 *Phys. Lett. A* **363** 507–11
- [29] Volkov V S, Bozhevolnyi S I, Rodrigo S G, Martín-Moreno L, García-Vidal F J, Devaux E and Ebbesen T W 2009 *Nano Lett.* **9** 1278–82
- [30] Berweger S, Atkin J M, Olmon R L and Raschke M B 2012 *J. Phys. Chem. Lett.* **3** 945–52
- [31] Tang L, Kocabas S E, Latif S, Okyay A K, Ly-Gagnon D S, Saraswat K C and Miller D A B 2008 *Nature Photon.* **2** 226–9
- [32] Schwarz S E and Ulrich B T 1977 *J. Appl. Phys.* **48** 1870
- [33] Wilke I and Herrmann W 1994 *Appl. Phys. B* **95** 87–95
- [34] Fumeaux C 2000 *Infrared Phys. Technol.* **41** 271–81
- [35] González F and Boreman G 2005 *Infrared Phys. Technol.* **46** 418–28
- [36] Haes A, Hall W, Chang L and Klein W 2004 *Nano Lett.* **4** 1029
- [37] Anker J, Hall W, Lyandres O and Shah N 2008 *Nature Mater.* **7** 442
- [38] Kabashin A V, Evans P, Pastkovsky S, Hendren W, Wurtz G A, Atkinson R, Pollard R, Podolskiy V A and Zayats A V 2009 *Nature Mater.* **8** 867–71
- [39] Ropers C, Neacsu C C, Elsaesser T, Albrecht M, Raschke M B and Lienau C 2007 *Nano Lett.* **7** 2784–8
- [40] Huang J S J, Feichtner T, Biagioni P and Hecht B 2009 *Nano Lett.* **9** 1897–902
- [41] Wen J, Romanov S and Peschel U 2009 *Opt. Express* **17** 5925–32
- [42] Neacsu C C, Berweger S, Olmon R L, Saraf L V L, Ropers C and Raschke M B 2010 *Nano Lett.* **10** 592–6
- [43] Krenz P M, Olmon R L, Lail B A, Raschke M B and Boreman G D 2010 *Opt. Express* **18** 21678–86
- [44] Berweger S, Atkin J M, Xu X G, Olmon R L and Raschke M B 2011 *Nano Lett.* **11** 4309–13
- [45] Farahani J N, Pohl D W, Eisler H J and Hecht B 2005 *Phys. Rev. Lett.* **95** 017402
- [46] Taminiau T, Moerland R, Segerink F, Kuipers L and van Hulst N 2007 *Nano Lett.* **7** 28–33
- [47] Taminiau T H, Stefani F D and van Hulst N F 2008 *Opt. Express* **16** 10858–6
- [48] Taminiau T H, Stefani F D, Segerink F B and van Hulst N F 2008 *Nature Photon.* **2** 234–7
- [49] Berweger S, Atkin J M, Olmon R L and Raschke M B 2010 *J. Phys. Chem. Lett.* **1** 3427–32
- [50] Bonod N, Devilez A, Rolly B, Bidault S and Stout B 2010 *Phys. Rev. B* **82** 115429
- [51] Rolly B, Stout B, Bidault S and Bonod N 2011 *Opt. Lett.* **36** 3368–70
- [52] Neubrech F, Pucci A, Cornelius T, Karim S, García-Etxarri A and Aizpurua J 2008 *Phys. Rev. Lett.* **101** 157403
- [53] Bharadwaj P, Beams R and Novotny L 2011 *Chem. Sci.* **2** 136

- [54] Sönnichsen C, Franzl T, Wilk T, von Plessen G and Feldmann J 2002 *Phys. Rev. Lett.* **88** 077402
- [55] Sönnichsen C, Franzl T, Wilk T, von Plessen G and Feldmann J 2002 *New J. Phys.* **4** 93
- [56] Buchler B, Kalkbrenner T, Hettich C and Sandoghdar V 2005 *Phys. Rev. Lett.* **95** 063003
- [57] Kühn S, Håkanson U, Rogobete L and Sandoghdar V 2006 *Phys. Rev. Lett.* **97** 017402
- [58] Dahmen C, Schmidt B and von Plessen G 2007 *Nano Lett.* **7** 318–22
- [59] Rogobete L, Kaminski F, Agio M and Sandoghdar V 2007 *Opt. Lett.* **32** 1623–5
- [60] Kinkhabwala A, Yu Z, Fan S, Avlasevich Y, Müllen K and Moerner W E 2009 *Nature Photon.* **3** 654–7
- [61] Greffet J J, Laroche M and Marquier F 2010 *Phys. Rev. Lett.* **105** 117701
- [62] Koenderink A F 2010 *Opt. Lett.* **35** 4208–10
- [63] Seok T J *et al* 2011 *Nano Lett.* **11** 2606–10
- [64] Kats M A, Yu N, Genevet P, Gaburro Z and Capasso F 2011 *Opt. Express* **19** 21748–53
- [65] Frimmer M, Chen Y and Koenderink A F 2011 *Phys. Rev. Lett.* **107** 123602
- [66] Purcell E M 1946 Spontaneous emission probabilities at radio frequencies *Proc. American Physical Society (Hamilton, NY)* p 681
- [67] Jackson J D 1998 *Classical Electrodynamics* 3rd edn (New York: Wiley)
- [68] Born M and Wolf E 1964 *Principles of Optics* 2nd edn (New York: Macmillan)
- [69] Nilsson J W and Riedel S 2010 *Electric Circuits* 9th edn (Upper Saddle River, NJ: Prentice-Hall)
- [70] King R W P 1956 *Theory of Linear Antennas* (Cambridge, MA: Harvard University Press)
- [71] Kraus J D 1950 *Antennas* (New York: McGraw-Hill)
- [72] Alù A and Engheta N 2008 *Phys. Rev. B* **78** 195111
- [73] Novotny L and Hecht B 2006 *Principles of Nano-optics* (New York: Cambridge University Press)
- [74] Fowles G R 1989 *Introduction to Modern Optics* 2nd edn (Mineola, NY: Dover)
- [75] Liu M, Pelton M and Guyot-Sionnest P 2009 *Phys. Rev. B* **79** 35418
- [76] Wissman P and Finzel H U 2007 *Electrical Resistivity of Thin Metal Films* (Berlin: Springer)
- [77] Palik E D (ed) 1998 *Handbook of Optical Constants of Solids* (New York: Academic)
- [78] Thèye M L 1970 *Phys. Rev. B* **2** 3060
- [79] Johnson P B and Christy R W 1972 *Phys. Rev. B* **6** 4370
- [80] Olmon R L, Slovick B, Johnson T W, Shelton D, Oh S H, Boreman G D and Raschke M B 2012 in preparation
- [81] Raether H 1988 *Surface Plasmons on Smooth and Rough Surfaces and on Gratings* (Berlin: Springer)
- [82] Barnes W, Dereux A and Ebbesen T 2003 *Nature* **424** 824–30
- [83] Ishimaru A 1991 *Electromagnetic Wave Propagation, Radiation, and Scattering* (Englewood Cliffs, NJ: Prentice-Hall)
- [84] Knight M W, Grady N K, Bardhan R, Hao F, Nordlander P and Halas N J 2007 *Nano Lett.* **7** 2346–50
- [85] Dorfmueller J, Vogelgesang R, Weitz R, Rockstuhl C, Etrich C, Pertsch T, Lederer F and Kern K 2009 *Nano Lett.* **9** 2372–7
- [86] Cubukcu E and Capasso F 2009 *Appl. Phys. Lett.* **95** 201101
- [87] Taminiau T H, Stefani F D and van Hulst N F 2011 *Nano Lett.* **11** 1020–4
- [88] Novotny L 2007 *Phys. Rev. Lett.* **98** 266802
- [89] Bryant G, García de Abajo F J and Aizpurua J 2008 *Nano Lett.* **8** 631–6
- [90] Encina E R and Coronado E A 2007 *J. Phys. Chem. C* **111** 16796–801
- [91] Locatelli A, Boscolo S and Capobianco A D 2011 *IEEE Photon. Technol. Lett.* **23** 1541–3
- [92] Muskers O and Giannini V 2007 *Opt. Express* **15** 17736–46
- [93] Crozier K B, Sundaramurthy A, Kino G S and Quate C F 2003 *J. Appl. Phys.* **94** 4632
- [94] Neubrech F, Weber D, Lovrincic R, Pucci A, Lopes M, Toury T and de La Chapelle M L 2008 *Appl. Phys. Lett.* **93** 163105
- [95] Aksu S, Yanik A A, Adato R, Artar A, Huang M and Altug H 2010 *Nano Lett.* **10** 2511–8
- [96] Mühlischlegel P, Eisler H J, Martin O J F, Hecht B and Pohl D W 2005 *Science* **308** 1607–9
- [97] Olmon R L, Krenz P M, Jones A C, Boreman G D and Raschke M B 2008 *Opt. Express* **16** 20295–305
- [98] Jones A C, Olmon R L, Skrabalak S E, Wiley B J, Xia Y N and Raschke M B 2009 *Nano Lett.* **9** 2553–8
- [99] Schnell M, Huber A J, Crozier K, Aizpurua J and Hillenbrand R 2009 *Nature Photon.* **3** 287–91
- [100] Alù A and Engheta N 2008 *Phys. Rev. Lett.* **101** 043901
- [101] Alù A and Engheta N 2008 *Nature Photon.* **2** 307–10
- [102] Locatelli A, De Angelis C, Modotto D, Boscolo S, Sacchetto F, Midrio M, Capobianco A D, Pigozzo F M and Smeda C G 2009 *Opt. Express* **17** 16792–800
- [103] De Angelis C, Locatelli A, Modotto D and Boscolo S 2010 *J. Opt. Soc. Am. B* **27** 997–1001
- [104] Chen P Y and Alù A 2010 *Phys. Rev. B* **82** 235405
- [105] Zhao Y, Engheta N and Alù A 2011 *J. Opt. Soc. Am. B* **28** 1266–74
- [106] Duan H, Fernandez-Dominguez A I, Bosman M, Maier S A and Yang J K W 2012 *Nano Lett.* **12** 3334–8
- [107] Burke P J, Li S and Yu Z 2006 *IEEE Trans. Nanotechnol.* **5** 314–34
- [108] Berthelot J *et al* 2009 *Nano Lett.* **9** 3914–21
- [109] Aizpurua J, Bryant G W, Richter L J and García de Abajo F J 2005 *Phys. Rev. B* **71** 235420
- [110] Pohl D W, Rodrigo S G and Novotny L 2011 *Appl. Phys. Lett.* **98** 023111
- [111] Maksymov I S, Miroshnichenko A E and Kivshar Y S 2011 Tunable plasmonic Yagi-Uda nanoantenna *International Workshop on Nonlinear Photonics (NLP) (Kharkov)* pp 1–3
- [112] Alù A and Engheta N 2010 *Phys. Rev. Lett.* **104** 213902
- [113] Fang Z, Fan L, Lin C, Zhang D, Meixner A J and Zhu X 2011 *Nano Lett.* **11** 1676–80
- [114] Bean J A, Weeks A, Member S and Boreman G D 2011 *IEEE J. Quantum Electron.* **47** 126–35
- [115] Grynberg G, Aspect A and Fabre C 2010 *Introduction to Quantum Optics* (New York: Cambridge University Press)
- [116] Thornton S T and Rex A 2005 *Modern Physics for Scientists and Engineers* (Boston, MA: Brooks/Cole)
- [117] Hilborn R C 1981 *Am. J. Phys.* **50** 982
- [118] Fujimoto T, Goto C and Fukuda K 1982 *Phys. Scr.* **26** 443–50
- [119] Stiles P L, Dieringer J A, Shah N C and Van Duyne R P 2008 *Annu. Rev. Anal. Chem.* **1** 601–26
- [120] Wokaun A and Gordon J 1982 *Phys. Rev. Lett.* **48** 957–60
- [121] Hanke T, Cesar J, Knittel V, Trügler A, Hohenester U, Leitenstorfer A and Bratschkitsch R 2012 *Nano Lett.* **12** 992–6
- [122] Anderson A, Deryckx K S, Xu X G, Steinmeyer G and Raschke M B 2010 *Nano Lett.* **10** 2519–24
- [123] Yifat Y, Iluz Z, Eitan M, Friedler I, Hanein Y, Boag A and Scheuer J 2012 *Appl. Phys. Lett.* **100** 111113
- [124] Miller E K and Landt J A 1980 *Proc. IEEE* **68** 1396
- [125] Pohl D W 2001 Near-field optics and the surface plasmon polariton *Topics in Applied Physics* vol 81, ed S Kawata (Berlin: Springer) pp 1–13
- [126] Drexhage K 1970 *J. Lumin.* **2** 693–701

- [127] Chance R R, Prock A and Silbey R 1978 Molecular fluorescence and energy transfer near interfaces *Advances in Chemical Physics* vol 37, ed I Prigogine and S A Rice (New York: Wiley) pp 1–65
- [128] Anger P, Bharadwaj P and Novotny L 2006 *Phys. Rev. Lett.* **96** 3–6
- [129] Sun G, Khurgin J B and Yang C C 2009 *Appl. Phys. Lett.* **95** 171103
- [130] Xu X G and Raschke M B, in preparation
- [131] Derom S, Vincent R, Bouhelier A and Colas-des Francs G 2012 *Europhys. Lett.* **98** 47008
- [132] Giannini V, Fernández-Domínguez A I, Sonnefraud Y, Roschuk T, Fernández-García R and Maier S A 2010 *Small* **6** 2498–507
- [133] Stockman M, Faleev S and Bergman D 2002 *Phys. Rev. Lett.* **88** 067402
- [134] Aeschlimann M, Bauer M, Bayer D, Brixner T, García de Abajo F J, Pfeiffer W, Rohmer M, Spindler C and Steeb F 2007 *Nature* **446** 301–4
- [135] Volpe G, Molina-Terriza G and Quidant R 2010 *Phys. Rev. Lett.* **105** 216802
- [136] Kao T S, Rogers E T F, Ou J Y and Zheludev N I 2012 *Nano Lett.* **12** 2728–31
- [137] Issa N A and Guckenberger R 2007 *Plasmonics* **2** 31–7
- [138] De Angelis F *et al* 2010 *Nature Nanotechnol.* **5** 67–72
- [139] Sadiq D, Shirdel J, Lee J S, Selishcheva E, Park N and Lienau C 2011 *Nano Lett.* **11** 1609–13
- [140] Mosk A P, Lagendijk A, Lerosy G and Fink M 2012 *Nature Photon.* **6** 283
- [141] Verhagen E, Spasenović M, Polman A and Kuipers L 2009 *Phys. Rev. Lett.* **102** 203904
- [142] Schnell M, Alonso-Gonzalez P, Arzubiaga L, Casanova F, Hueso L, Chuvilin A and Hillenbrand R 2011 *Nature Photon.* **5** 283–7
- [143] Atay T, Song J H and Nurmikko A V 2004 *Nano Lett.* **4** 1627–31
- [144] Adato R, Yanik A A and Altug H 2011 *Nano Lett.* **11** 5219–26
- [145] Pavlov R S, Curto A G and van Hulst N F 2012 *Opt. Commun.* **285** 3334–40
- [146] Curto A G, Volpe G, Taminiau T H, Kreuzer M P, Quidant R and van Hulst N F 2010 *Science* **329** 930–3
- [147] Schuck P J, Fromm D P, Sundaramurthy A, Kino G S and Moerner W E 2005 *Phys. Rev. Lett.* **94** 017402
- [148] Kino G S, Sundaramurthy A, Schuck P J, Fromm D P and Moerner W E 2007 Optical field enhancement with plasmon resonant bowtie nanoantennas *Surface Plasmon Nanophotonics* ed M L Brongersma and P G Kik (Dordrecht: Springer) pp 125–37
- [149] Fumeaux C, Boreman G D, Herrmann W, Rothuizen H and Kneubühl F K 1997 *Appl. Opt.* **36** 6485
- [150] Barnard E S, Pala R A and Brongersma M L 2011 *Nature Nanotechnol.* **6** 588–93
- [151] Chaturvedi P, Hsu K, Kumar A and Fung K 2009 *ACS Nano* **3** 2965–74
- [152] Vogelgesang R and Dmitriev A 2010 *Analyst* **135** 1175–81
- [153] Lewis A, Isaacson M, Harootunian A and Muray A 1984 *Ultramicroscopy* **13** 227–31
- [154] Pohl D W, Denk W and Lanz M 1984 *Appl. Phys. Lett.* **44** 651
- [155] Betzig E and Trautman J K 1992 *Science* **257** 189–95
- [156] Bachelot R, Gleyzes P and Boccard A C 1994 *Microsc. Microanal. Microstruct.* **5** 389–97
- [157] Zenhausern F, OBoyle M P and Wickramasinghe H K 1994 *Appl. Phys. Lett.* **65** 1623
- [158] Keilmann F and Hillenbrand R 2004 *Phil. Trans. R. Soc. A* **362** 787–806
- [159] Bek A, Vogelgesang R and Kern K 2006 *Rev. Sci. Instrum.* **77** 043703
- [160] Raschke M B, Molina L, Elsaesser T, Kim D, Knoll W, Hinrichs K and Kim H 2005 *ChemPhysChem* **6** 2197–203
- [161] Wang K, Mittleman D M, van der Valk N C J and Planken P C M 2004 *Appl. Phys. Lett.* **85** 2715
- [162] Keilmann F, Huber A J and Hillenbrand R 2009 *J. Infrared Milli Terahertz Waves* **30** 1255–68
- [163] Alonso-Gonzalez P *et al* 2011 *Nano Lett.* **11** 3922–6
- [164] Dorfmueller J, Dregely D, Esslinger M, Khunsin W, Vogelgesang R, Kern K and Giessen H 2011 *Nano Lett.* **11** 2819–24
- [165] Baudry D, Arcambal C, Louis A, Mazari B and Eudeline P 2007 *IEEE Trans. Electromag. Compatib.* **49** 485–93
- [166] Imtiaz A, Wallis T M, Lim S H, Chisum J, Popovic Z and Kabos P 2010 Near-field antenna as a scanning microwave probe for characterization of materials and devices *Proc. 4th European Conf. on Antennas and Propagation (EuCAP), 2010 vol 2 (Barcelona Spain)* pp 1–3
- [167] Olmon R L, Rang M, Krenz P M, Lail B A, Saraf L V, Boreman G D and Raschke M B 2010 *Phys. Rev. Lett.* **105** 167403
- [168] Seo M A, Adam A J L, Kang J H, Lee J W, Jeoung S C, Park Q H, Planken P C M and Kim D S 2007 *Opt. Express* **15** 11781–9
- [169] Grosjean T, Ibrahim I A, Suarez M A, Burr G W, Mivelle M and Charrat D 2010 *Opt. Express* **18** 5809
- [170] Lee K G *et al* 2007 *Nature Photon.* **1** 53–6
- [171] Schnell M, Garcia-Etxarri A, Alkorta J, Aizpurua J and Hillenbrand R 2010 *Nano Lett.* **10** 3524–8
- [172] Devaux E, Dereux A, Bourillot E, Weeber J C, Lacroute Y, Gouonnet J P and Girard C 2000 *Phys. Rev. B* **62** 10504–14
- [173] Burresti M, van Oosten D, Kampfrath T, Schoenmaker H, Heideman R, Leinse A and Kuipers L 2009 *Science* **326** 550–3
- [174] Jones A C and Raschke M B 2012 *Nano Lett.* **12** 1475–81
- [175] Dean R N, Nordine P C and Christodoulou C G 2000 3-D Helical THz antennas *Microw. Opt. Technol. Lett.* **24** 106